



## RESEARCH ARTICLE

10.1029/2022GC010788

### Key Points:

- The distance from the plume center is not the only factor controlling tectonic and volcanic activity along the Reykjanes Ridge
- Fault dimensions are primarily controlled by the variation of crustal thermal structure with distance from the hotspot
- Flat-topped seamount abundances peak where a V-shaped ridge intersects the axis, consistent with a buoyant upwelling melting instability

### Supporting Information:

Supporting Information may be found in the online version of this article.

### Correspondence to:

M. Le Saout,  
[mlesaut@geomar.de](mailto:mlesaut@geomar.de)

### Citation:

Le Saout, M., Pałgan, D., Devey, C. W., Lux, T. S., Petersen, S., Thorhallsson, D., et al. (2023). Variations in volcanism and tectonics along the hotspot-influenced Reykjanes Ridge. *Geochemistry, Geophysics, Geosystems*, 24, e2022GC010788. <https://doi.org/10.1029/2022GC010788>

Received 14 NOV 2022

Accepted 7 MAR 2023

## Variations in Volcanism and Tectonics Along the Hotspot-Influenced Reykjanes Ridge

M. Le Saout<sup>1</sup> , D. Pałgan<sup>2</sup> , C. W. Devey<sup>1</sup> , T. S. Lux<sup>1</sup>, S. Petersen<sup>1</sup>, D. Thorhallsson<sup>3</sup>, A. Tomkowicz<sup>2</sup>, and S. Brix<sup>4</sup>

<sup>1</sup>GEOMAR Helmholtz Centre for Ocean Research Kiel, Kiel, Germany, <sup>2</sup>Institute of Oceanography, University of Gdańsk, Gdańsk, Poland, <sup>3</sup>Hawai'i Institute of Geophysics and Planetology, Honolulu, HI, USA, <sup>4</sup>Senckenberg am Meer, German Centre for Marine Biodiversity Research (DZMB) c/o Biocenter Grindel, Hamburg, Germany

**Abstract** Mapping and sampling four sections of the slow-spreading Reykjanes Ridge provide insight into how tectonic and volcanic activity varies with distance from the Iceland plume. The studied areas are characterized by significant variations in water depth, lava chemistry, crustal thickness, thermal structure, and ridge morphology. For each study area, fault pattern and dimension, tectonic strain, seamount morphology, and density are inferred from 15 m-resolution bathymetry. These observations are combined with geochemical analysis from glass samples and sediment thickness estimations along Remotely Operated Vehicle-dive videos. They reveal that (a) tectonic and volcanic activity along the Reykjanes Ridge, do not systematically vary with distance from the plume center. (b) The tectonic geometry appears directly related to the deepening of the brittle/ductile transition and the maximum change in tectonic strain related to the rapid change in crustal thickness and the transition between axial-high and axial valley (~59.5°N). (c) Across-axis variations in the fault density and sediment thickness provide similar widths for the neo-volcanic zone except in regions of increased seamount emplacement. (d) The variations in seamount density (especially strong for flat-topped seamounts) are not related to the distance from the plume but appear to be correlated with the interaction between the V-shape ridges (VSR) flanking the ridge and the ridge axis. These observations are more compatible with the buoyant upwelling melting instability hypothesis for VSR formation and suggest that buoyant melting instabilities create many small magma batches which by-pass the normal subaxial magmatic plumbing system, erupting over a wider-than-normal area.

**Plain Language Summary** Volcanic eruptions and faults growth are two important geologic processes taking place along seafloor spreading centers. Their variations in space and time are displayed in the morphology of the spreading centers. Investigating these morphological variations is key to understanding the deeper processes of the oceanic crust formation. South of Iceland, the Reykjanes Ridge is the location of increased volcanism due to the interaction between the mid-ocean ridge and the Iceland hotspot. Using high-resolution seafloor topographic data, chemical analyses of volcanic rock, and videos of the seafloor from a remotely operated vehicle, we investigated how volcanism and faulting change along the ridge. The increase in fault dimensions (height, length) with distance from the plume center is probably the result of the crust and mantle becoming cooler and stiffer and thus able to support larger faults. Fault density and thickness of the sediment covering the lava flows near the ridge axis are used to delimit the region of young volcanism. Seamounts often emplaced beyond that region. A peak in seamount abundance near 60°N suggests that the thick crust here is generated from numerous small batches of magma possibly resulting from a migrating instability in the melt production process beneath the axis.

## 1. Introduction

Hotspots influence 15%–20% of global mid-ocean ridges (Ito et al., 2003), modifying both their geophysical and geomorphological characteristics (leading, e.g., to elevated topography, negative gravity anomalies, anomalous crustal production, e.g., Ito & Lin, 1995; Ito et al., 2003; Nadin et al., 1995; Richards et al., 1988; White et al., 1995) as well as their magma composition (producing anomalies in noble gas and radiogenic isotope ratios, and variation in trace element concentrations, e.g., Detrick et al., 2002; Hanan et al., 1986, 2000; Ito et al., 2003; Keller et al., 2000; Sinton et al., 2003; R. N. Taylor et al., 1995). The effect of hotspot-ridge interaction on mantle temperature, magma production, and magma composition has a direct influence on tectonic and volcanic processes, with Colman et al. (2012) and McClinton et al. (2013), for example, showing that along the Galapagos

© 2023. The Authors.

This is an open access article under the terms of the [Creative Commons Attribution License](https://creativecommons.org/licenses/by/4.0/), which permits use, distribution and reproduction in any medium, provided the original work is properly cited.

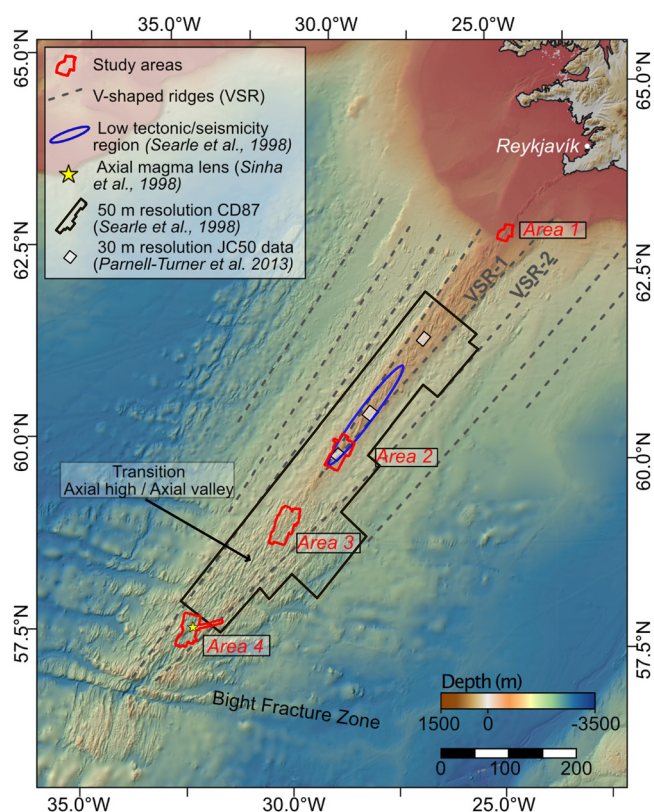


**Figure 1.** Map of the Reykjanes Ridge from the Bight Fracture Zone (~57°N) to the Reykjanes Peninsula (~63.5°N). The red boxes show the extent of the four areas studied in this paper (detailed map in Figure 2). V-shaped ridges (dashed lines) are located based on free-air gravity anomalies and named using the nomenclature from Jones et al. (2014). The axial magma lens evidenced by Sinha et al. (1998) is located by a yellow star. The 50 m resolution (CD87, Searle et al., 1998) and the section of the 30 m resolution data (JC50, Parnell-Turner et al., 2013) previously used to analyze tectonic variation along the axis are outlined in black. The low tectonic and seismic region defined by Searle et al. (1998) is shown by a blue oval.

Spreading Center, as the distance to the plume center increases, magma budgets decrease and eruptive temperatures increase. This is reflected in eruptions that are more voluminous away from the plume center but are dominated by pillow flows, while smaller but more frequent eruptions dominated by lobate and sheet flows are more common closer to the hotspot.

Of the 21 known and studied plume-ridge interaction, the Reykjanes Ridge shows hotspot-influence over the greatest along-axis distance (Ito, 2001). Thicker-than-average crust (Sinha et al., 1998; Weir et al., 2001), and enriched mid-ocean ridge basalts (e.g., Murton et al., 2002) are examples of the anomalies thought to show the transport of Iceland plume material over several hundreds of kilometers southward along the Reykjanes Ridge (Hart et al., 1973; Murton et al., 2002; Schilling, 1973a, 1973b; Schilling et al., 1983; Sun et al., 1975). As magma budget, lava chemistry, and thermal structure vary with distance from the hotspot (e.g., White et al., 1995), the Reykjanes Ridge is an ideal location to observe the effects of a plume on accretion processes along the ridge axis. Previous studies (Magde & Smith, 1995; Murton & Parson, 1993; Parnell-Turner et al., 2013; Parson et al., 1993; Searle et al., 1998) have used bathymetric data to look at volcanic and tectonic patterns along the Reykjanes Ridge and found that they do not appear to vary only with distance from the plume center, in contrast to what is observed along the Galapagos Spreading Center or in other plume-ridge interaction systems. However, these studies were based either on large-area but low-resolution data (~100 m bathymetric grid; Magde & Smith, 1995; Searle et al., 1998) or had a higher resolution (~30 m grid spacing) but over a relatively small area (<6% of the ridge length; Parnell-Turner et al., 2013).

Additionally, a unique feature of the Reykjanes Ridge and its surrounding seafloor is a pattern of “V-shaped ridges” (Vogt, 1971), which mark regions of thickened crust apparently generated at the spreading axis and whose sources appear to have migrated rapidly southward over time. Several explanations for the generation of the V-shaped ridges have been proposed, ranging from pulses of thermal anomalies that propagate away from the Iceland Plume (Parnell-Turner et al., 2013, 2017; Poore et al., 2011; Vogt, 1971), to propagating rifts (Hey et al., 2010) or propagation of robust upwelling instabilities originating from the mantle underlying the Reykjanes Ridge (e.g., Martinez & Hey, 2017). While some of the volcanic and tectonic variations along the Reykjanes ridges are proposed to result from VSR-ridge interactions (Magde & Smith, 1995; Parnell-Turner et al., 2013), such relationship is not well constrained.

This paper presents ship-based bathymetry data gridded at 15 m, geochemical data, and ground-truth observations from Remotely Operated Vehicle (ROV) dives collected at four regions along the Reykjanes Ridge, between 100 and 850 km from the Icelandic coast. We use these data to investigate the faulting pattern along and across the ridge axis as well as the distribution of seamounts and seamount morphotypes with respect of the neo-volcanic zone. Our goal is to analyze the variation of tectonic and volcanic processes with respect to distance from the hotspot in an attempt to provide additional geological constraints on mechanisms of hotspot-ridge interaction in this model system and shed light on the origin of the V-shaped ridges.

## 2. Geological Setting

The Reykjanes Ridge is a slow-spreading ridge extending from the Bight Fracture Zone (~56.5°N) to the Reykjanes Peninsula on Iceland (~63.5°N). It is the longest oblique spreading ridge on Earth (Höskuldsson et al., 2007) with a length of about 900 km (Figure 1). Its full spreading rate ranges from ~16.8 mm yr<sup>-1</sup>, near Iceland, to ~20.4 mm yr<sup>-1</sup> close to the Bight transform fault (Argus et al., 2011). The average spreading direction (~105°), oblique compared to the geographical bearing of the Reykjanes Ridge bathymetric feature (~036°) (DeMets et al., 1994), results in accretion organized in an “en echelon” array of Axial Volcanic Ridges (AVRs),



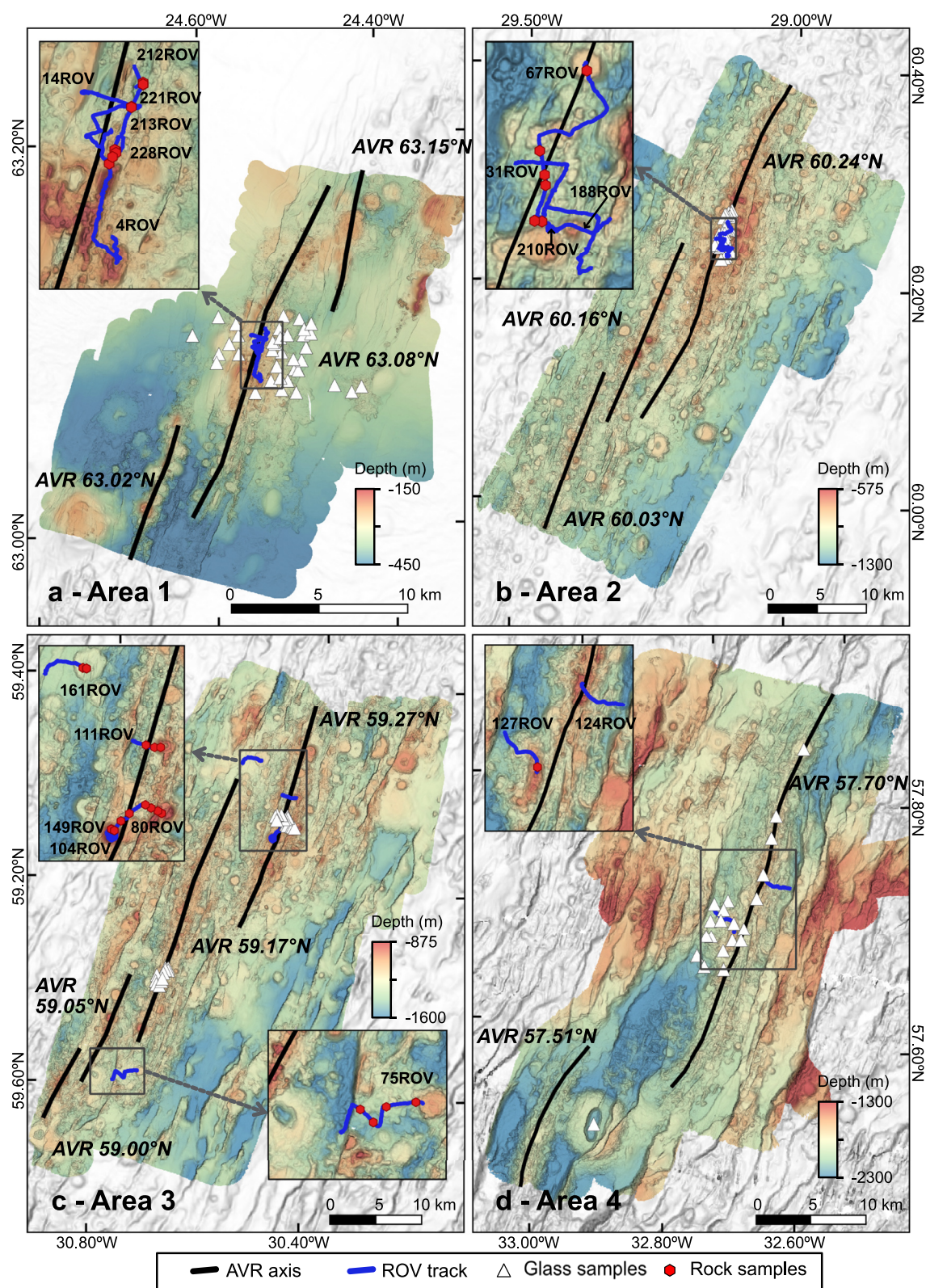


**Figure 2.** Bathymetric maps showing our data from the four study areas gridded at 15 m. Surrounding areas are shown with a gray-scale slope map extracted from the pre-existing lower resolution (>30 m) ship-based bathymetry. The location of the axis of the axial volcanic ridges is indicated by black lines labeled by the latitude at the center point. The Remotely Operated Vehicle (ROV) dives and the wax-coring stations are located by blue lines and white triangles, respectively. The insets show the location of the rock samples (red circles) collected during the ROV dives.

Searle & Laughton, 1981). Typical AVRs are 3–6 wide, 20–30 km long, 200–500 m high, and overlap with each other over a distance of, on average, 1/3 of their length (Höskuldsson et al., 2007; Keeton et al., 1997; Pałgan et al., 2017; Searle et al., 1998; Talwani et al., 1971).

The Reykjanes Ridge shows several unusual characteristics attributed to its interaction with the Iceland plume (Talwani et al., 1971; Vogt, 1971; White et al., 1995). The axis, uninterrupted by first-order discontinuities, shoals progressively from ~2,500 mbsl in the south (Keeton et al., 1997) to ~300 mbsl near 63°N (Höskuldsson et al., 2007; Pałgan et al., 2017) and eventually emerges above sea level on the Reykjanes Peninsula in Iceland (Sæmundsson, 1979). This is attributed to two effects, both linked to a higher potential temperature in the asthenosphere approaching Iceland (Poore et al., 2011; White et al., 1995). First, gradual thickening of the crust (from ~7.5 km near the BFZ (Sinha et al., 1998) to ~14 km at the Icelandic coast (Weir et al., 2001; White et al., 1995)) due to higher magma production rates close to the plume. This thickening might be related to more frequent and/or more voluminous eruptions. Second, a decrease in mantle density at the higher temperatures closer to the plume center (Höskuldsson et al., 2007; White et al., 1995), resulting in the uplift of the ridge by thermal buoyancy (White et al., 1995). The presumed variations in magmatic input and thermal buoyancy along the ridge have also been used to explain the along-strike transition of axial morphology; from a 700 m deep and 8–13 km-wide axial valley in the south (Searle et al., 1998) to a prominent axial high in the north (with the transition lying at roughly 58°40'N) (Appelgate & Shor, 1994; Searle et al., 1998; Vogt, 1971).

Seismic reflection surveys conducted along some sections of the Reykjanes Ridge (Sinha et al., 1998) have only imaged one intracrustal magma body. The 4 km wide and 100 m thick magma lens lies at a depth of 2.5 km underneath the AVR located at ~57°45'N. The rough hummocky terrain, strong acoustic backscatter, and relatively fresh-looking lava flows on the AVR, together with little indication of extensive tectonic deformation, were interpreted as indicating that the magma lens underlies a region of young volcanic activity (Sinha et al., 1998).

Despite suggested excess magmatism, and hence, heat input into the ridge system, the Reykjanes Ridge is characterized by an apparent paucity of high-temperature hydrothermal vents with presently only two known vent fields: the Steinahóll (~63°06'N) and IceAGE (~60°N) hydrothermal fields (Brix et al., 2020; German et al., 1994; J. Taylor et al., 2021).

Free-air gravity gradient data and seismic reflection profiles (Parnell-Turner et al., 2017) have shown the presence of V-shaped ridges (VSR) on each side of the Reykjanes Ridges (Figure 1). Two VSR intersect the ridge axis: VSR-1 at ~60°N (Magde & Smith, 1995; Parnell-Turner et al., 2013; Searle et al., 1998; Vogt, 1971) and VSR-2 at ~57°N close to the Bight transform fault (Jones et al., 2014). VSRs are associated with low incompatible element concentrations and ratios in axial magmas (Jones et al., 2014) and are suggested to be the locus of increased magmatic activity with apparent thickening of the crust (Smallwood & White, 1998). The intersection of the ridge and VSR-1 is marked by a higher density of seamounts (Magde & Smith, 1995), with simultaneous reduction of fault density and seismicity (Figure 1, Parnell-Turner et al., 2013; Searle et al., 1998).

### 3. Data and Methods

#### 3.1. Data

Four sections of the Reykjanes Ridge were mapped and sampled (Figure 1) in 2018 during the research cruise MSM75 of the German Research Vessel “Maria S. Merian” (Devey et al., 2022). The bathymetry acquisition was carried out at a speed of 5 knots using the hull-mounted Kongsberg EM712 75 kHz echo-sounder. A total surface of ~5,000 km<sup>2</sup>, or 21% of the total ridge length, was mapped at a resolution of 5–15 m (depending on the average water depth, which varied from 300 to 2,300 m, respectively). The multibeam bathymetric data presented in the study (Devey et al., 2020) are available on the PANGAEA repository (<https://doi.org/10.1594/PANGAEA.922925>). The combined data were used to plan dives with the GEOMAR ROV “PHOCA” and to guide ship-based geological sampling. A total of 18 ROV dives were completed for an accumulative time of ~97 hr of seafloor observation. Geological samples were collected during ROV dives and 153 wax cores for a total of 29 rock and 142 glass samples, respectively (Figure 2).

#### 3.2. Methods

##### 3.2.1. Delineation and Measurement of Tectonic and Magmatic Features

As a basis for the volcanological and tectonic interpretation presented in this paper, we gridded data from all four areas at a common grid spacing of 15 m (Figure 2). We assume that seamounts (volcanoes) have a sub-circular



shape with a minimum height of 10 m. They were delineated by the slope change at the bottom of their flanks using bathymetry and slope maps. Faults were classified as linear vertical steps in bathymetry. Their location was defined as the base of their scarp. To investigate relative differences in the intensity of faulting, we calculated the parameter “fault density,” which is the total length of fault scarps found in a  $500 \times 500$  m cell, represented in units of km/km<sup>2</sup>. The 500 m cell size was chosen to correspond to the average spacing between fault lineaments so that most cells should have non-zero values (see Section 4.2). Similarly, the analysis of the along- and across-axis distribution of tectonic features was performed using profiles across the individual AVRs spaced at 500 m along-axis. Across-axis fault density was then averaged over all profiles across a particular AVR to obtain one mean variation per AVR. Finally, AVRs are delineated using the change of slope between the AVR-flank and the surrounding seafloor on the bathymetric maps (see Figure S1 in Supporting Information S1). AVR average geometry (maximum width and height) was determined for each AVR using the 500 m-spaced profiles, with width defined as the horizontal distance between the western and eastern bases and the height as the vertical distance between the average AVR base and its crest.

### 3.2.2. Determination of the Magmatic Extension

To characterize the tectono-volcanic variation along the Reykjanes Ridge axis, we estimate the fraction ( $M$ ) of extension accommodated by magmatic accretion as defined by Behn and Ito (2008), where  $M = 1$  represents a wholly magmatic extension, and  $M = 0$  corresponds to amagmatic extension.  $M$  is calculated as 1 minus the fraction of extension accommodated by faulting. This tectonic extension, in turn, was calculated from across-axis profiles (a total of seventy-two cross-axis profiles, 18 per working area) using the cumulative horizontal displacement as a function of the distance between the two most distant faults, following the procedure presented by Howell et al. (2016). To estimate the horizontal displacement from fault height, we need to estimate the fault dip. As shown in previous studies (e.g., Carbotte et al., 2003; Howell et al., 2016; Le Saout et al., 2018), erosion, mass wasting, and data resolution can affect estimations of the apparent fault dip and heave. The vertical resolution of our bathymetric data is much better than the horizontal resolution, so we determined fault heave using the measured scarp height (see method in Figure S2 in Supporting Information S1). As the fault slope itself is, in many cases, difficult to determine (see below), we assumed an original fault dip in the range  $55^\circ \pm 15^\circ$  which provided us with a range of tectonic extension values. We use a fixed dip angle to avoid overestimating the tectonic extension due to the data resolution in regions characterized by small fault heaves. Indeed, with 15 m resolution data, faults with heave <10 m will appear to have a dip < $55^\circ$ . The  $55^\circ \pm 15^\circ$  angle was chosen based on measured dips across the 72 profiles for faults with sufficient heave that a dip could be accurately determined (see justification in the data presented in Figure S3 in Supporting Information S1).

### 3.2.3. Determination of the Sediment Cover

ROV observations showed significant variation in sediment cover on the AVRs. To quantify this, we used the sedimentation scale from Yeo and Searle (2013) that consists of four visual categories: (a) a sediment cover <10% corresponds to a light dusting of sediment on the lava flows; (b) a sediment cover of 10%–50% signifies that sediment pockets are present on the seafloor, but they are not connected; (c) a sediment cover of 50%–90% corresponds to heavy sedimentation with interconnected sediment pocket; and (d) a sediment cover >90% is present when no or only a few lava outcrops are visible on an otherwise sedimented plain.

### 3.2.4. Major Element Analysis

The major element contents of glasses were determined on a JEOL JXA-8200 Superprobe electron microprobe at GEOMAR using a 15 kV accelerating voltage (Table S1). In total, 171 samples were analyzed. Matrix glasses were analyzed using a beam diameter of 5  $\mu$ m, 10 nA beam current, and VGA 99 (USNM 113498/1) and VG-2 (USNM 111240) as standards (Jarosewich, 2002). Peak and background counting times were generally 20 and 10 s, respectively (detailed analysis in Devey & Le Saout, 2023).

## 4. Results

### 4.1. Axial Volcanic Ridge Morphology

A total of 12 AVRs were mapped, five of them only partially (Figure 2). We named the AVRs based on the latitude at their center. The AVRs strike between  $019^\circ$  and  $027^\circ$ , parallel to the AVRs north of  $62.5^\circ$ N (Pałgan et al., 2017) and relatively perpendicular to the spreading direction ( $\sim 105^\circ$ , DeMets et al., 1994). Their dimensions (i.e., length,

**Table 1**  
*Characteristics of the Axial Volcanic Ridges*

Area	Latitude (°N)	Length <sup>a</sup> (m)	Height (m)	Width base (km)	Fraction overlapped (%)
1	63.15	7,998	53	3.44	84
	63.08	20,292	108	6.70	56
	63.02	7,878	157	2.11	59
2	60.24	37,204	176	5.38	49
	60.16	19,581	197	3.25	100
	60.03	16,822	155	3.75	25
3	59.27	25,136	195	4.71	57
	59.17	30,218	249	5.40	68
	59.05	12,387	365	5.62	70
	59.00	8,080	284	4.65	31
4	57.70	38,611	234	5.04	–
	57.51	14,092	352	4.23	–

<sup>a</sup>The length is indicated in red for AVR not entirely mapped.

width, and height, Table 1 and Figure S4 in Supporting Information S1) are similar to those which have previously been measured along other sections of the Reykjanes Ridge (Höskuldsson et al., 2007; Keeton et al., 1997; Paġan et al., 2017; Searle et al., 1998; Talwani et al., 1971). The fraction of overlapping AVR in our data set is higher than previously estimated along the Reykjanes Ridge. With the exception of the two southern-most AVRs, each AVR is overlapped over at least 50% of its entire length by at least one other AVR; the AVR at 60.16°N is entirely overlapped by the 60.24°N AVR. The two southern-most AVRs, although they do not overlap, show a slight bend of their axial tips toward each other (Figure 2d), a feature less evident on the other AVR.

## 4.2. Tectonic Pattern

More than 2,000 fractures were identified within the four working areas (Figure 3). The mean strike per area varies between 019° (northern part) and 025° (southern part) (Figure 3 and Table 2). Overall, the mean strike is parallel to the AVR axis orientation. Fault pattern and fault dimensions are not homogeneous along the ridge axis (Figure 4). Faults are, on average, longer, have a larger throw, and are more widely spaced toward the south (Figure 4, Table 2). This is confirmed by violin plots (Figures 4b and 4c) showing that the interquartile range (central 50% of the data set in each area) and the most

frequent fault length and height also increase toward the south. In contrast to the previous parameters, the fault density does not appear to follow any trend. It is the highest in Area 1, closely followed by Area 2 and reaches a minimum in Area 3 (Figure 4a, Table 2).

The fault distribution is also highly variable across the axis (Figure 5). The fault density is generally low at the axis but increases rapidly within the first 0.5–2.7 km. The region of increase is the narrowest in Area 2 (<1 km) and even non-existent in the case of the AVR 60.16°N. The fault density at the axis is usually higher (>0.7 km/km<sup>2</sup>) for AVRs with a summit plateau (e.g., AVR 59.57°N). The distance to either side of the axis where fault density increases is either symmetrical (e.g., AVR 63.02°N) or asymmetrical (e.g., AVR 57.70°N), independent of the AVR's cross-section morphology. Away from this region, the fault pattern oscillates between high and low density with a maximum fault density that decreases slowly with distance from the axis. This variation is especially noticeable in Areas 2 and 3 (Figure 5).

## 4.3. Morphology and Distribution of Volcanic Features

Within the four sections of the Reykjanes Ridge mapped, 571 seamounts were identified and measured (Figure 3). Their diameters are mostly less than 2 km (97%) but can reach up to 6.2 km (e.g., Area 4, Figures 2d and 3d). Although they are observed everywhere, there are regional variations in the number and density of seamounts. The seamount density is lower in Areas 1 and 4 (6.8% and 7.4% of the mapped areas, respectively) than in Areas 2 or 3 (13.7% and 10.7% of the mapped areas, respectively, see Table 2). Three primary seamount types (flat-topped, dome-shaped, and cone-shaped) can be distinguished based on their morphology. Their average basal diameter  $d$ , summit height  $h$ , and slope angle  $s$  (Figure 6) are used to characterize the different morphologies in a manner similar to that used by Augustin et al. (2016). Table 3 summarizes the average dimensions of each seamount morphotype. About 63% of the seamounts we surveyed are flat-topped volcanoes (Figure 6a) characterized by a 0.1–3.1 km basal diameter and a height up to 302 m, with an aspect ratio of  $0.13 \pm 0.04$  (Figure 6d). Flat-topped volcanoes are characterized by abrupt changes in the slope between the summit and the flank. Their flank slope varies from 9° to 29° with an average angle of 18°. Their dimensions and height-to-diameter ratio are similar to those previously observed along the Red Sea and in Hawaii (Augustin et al., 2016; Clague et al., 2000). Their summit area is generally not smooth and clearly displays collapses, pressure ridges or well-defined flow lobes (Figure S5 in Supporting Information S1). Along the Reykjanes Ridge, the density of flat-topped volcanoes ranges between 32 and 169 volcanoes per 1,000 km<sup>2</sup>, with a maximum reached in Area 2 (Figure 7b). Dome-shaped seamounts (Figure 6c) are the second most common type of seamount (20%), with diameter and height reaching 6.2 km and 356 m, respectively, and an aspect ratio of  $0.06 \pm 0.02$  (Figure 6d). While their flank

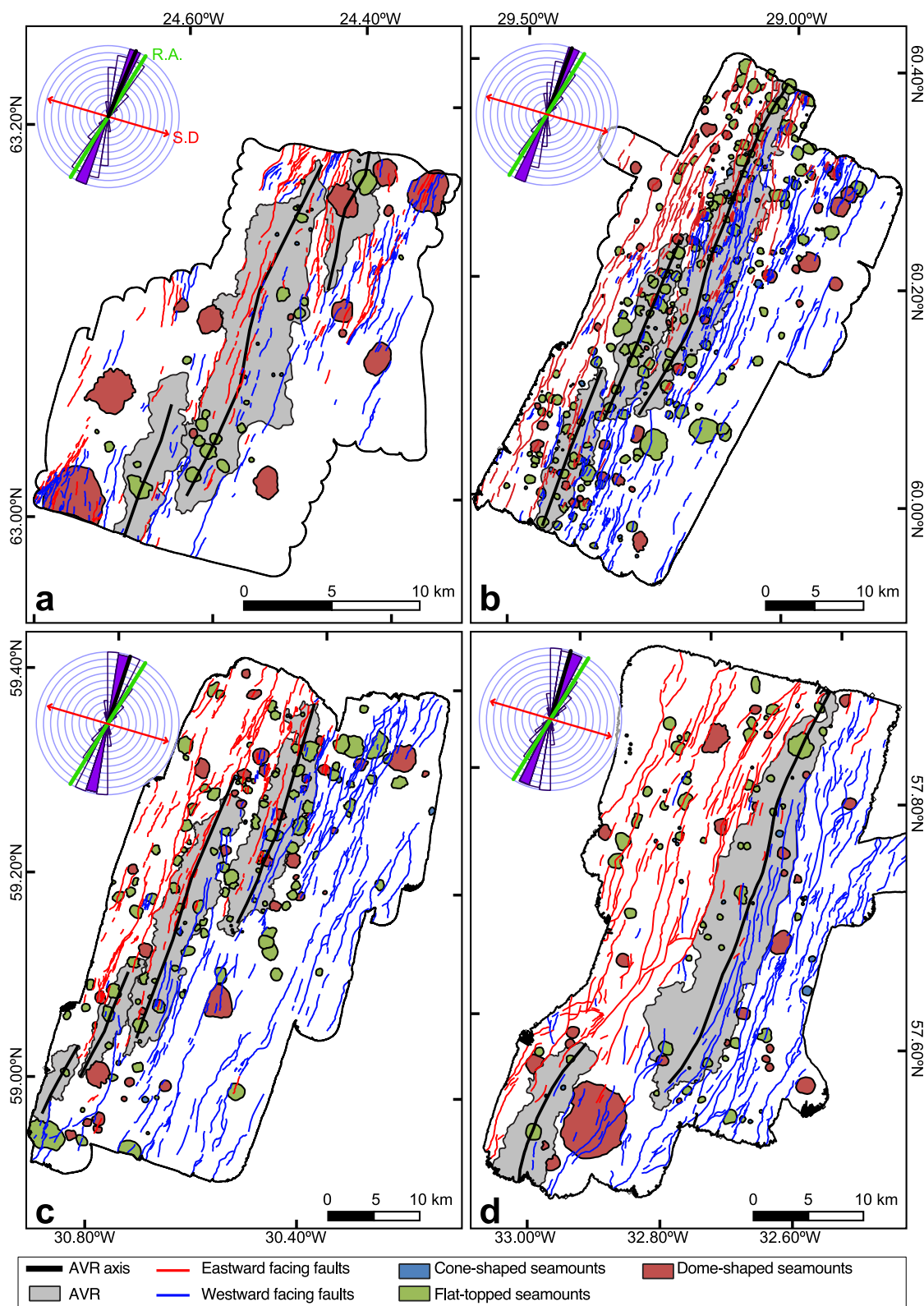


**Figure 3.** Structural map of (a) Area 1, (b) Area 2, (c) Area 3, and (d) Area 4 based on our new data. Axial Volcanic Ridges (AVRs) are shaded in gray, and their axis is marked by a bold black line. Westward- and eastward-facing faults are delineated in blue and red, respectively. Seamounts are colored based on their morphology: flat-topped seamounts in green, cone-shaped seamounts in blue, and dome-shaped seamounts in red. The rose diagrams indicate the fault orientations by area, with an interval of 9°, and the mean bearing is shown in purple. The AVR orientation, the global ridge axis (R.A.) orientation, and the spreading direction (S.D.) are shown in the rose diagram by a black, green, and red axis, respectively.

**Table 2**  
*Fault Dimensions and Distribution by Area*

Area name	Surface mapped (km <sup>2</sup> )	Fault number	Fault statistics					Fault strain (%) <sup>a</sup>		
			Length (m)		Density (km/km <sup>2</sup> )	Mean strike (°N)	Mean fault spacing (m)	Dip (°)		
			(Range)	(Mean)				40	55	70
1	366.31	394	92–5,496	802	0.86	25 ± 1.1	349	2.18	1.28	0.67
2	1,142.02	738	115–9,157	1,308	0.84	19.3 ± 0.7	559	5.10	2.99	1.56
3	1,523.20	507	170–12,286	1,880	0.61	19.3 ± 1.1	759	6.64	3.90	2.03
4	1,289.32	399	193–20,603	2,449	0.74	21.3 ± 1.7	875	11.87	6.98	3.63

<sup>a</sup>Average fault strain determined along 20 bathymetric profiles perpendicular to the AVR axis.

slopes, ranging from 5° to 25° with a mean slope of 14°, are relatively similar to those of flat-topped seamounts, dome-shaped seamounts show a progressive transition between the summit area and the flank. Cone-shaped volcanoes (Figure 6b) are the least common type, comprising only 16.5% of the total seamounts. They are the smallest seamounts (<1.2 km in diameter), but have the largest aspect ratio (0.21, Figure 6d and Table 4) and steepest flanks (up to 40° with a mean slope of ~25°). The distributions of dome-shaped and cone-shaped seamounts are more homogeneous along the ridge and show no trend. Their density ranges are 0–44 and 18–44 seamounts per 1,000 km<sup>2</sup>, respectively (Figures 7c and 7d). About 16% of the seamounts have a crater at their summit, irrespective of seamount morphology or their position along the ridge axis.

#### 4.4. Geochemical Results

Major element geochemical results for the 142 glass samples collected in the four working areas are shown in Figures 7b and 7c, together with previously published data extracted from the PetDB database [www.earthchem.org/PetDB](http://www.earthchem.org/PetDB) (in November 2019, see the references for background data section in Supporting Information S1). In terms of MgO contents, the samples reported here fit into the trend of increasing MgO with distance from Iceland seen in published results (Figure 7e). With the exception of Area 4, the K<sub>2</sub>O/TiO<sub>2</sub> ratio of our samples is also similar to the previous measure, with most variations occurring in the northern section of the ridge (north of ~60.5°N). Our samples from Area 4 have similar ratios to those from Areas 2 (0.032–0.054) and 3 (0.031–0.052), but they are somewhat lower than previously reported in this area (e.g., Murton et al., 2002), with ratios ranging from 0.034 to 0.047 and 0.044 to 0.126, respectively (Figure 7f).

#### 4.5. Sediment Cover

The 19 ROV dives surveyed sections of 5 of the 12 mapped AVRs (Figure 2). Figure 8a shows the distribution of sediment cover over a distance of up to ~7 km from the axis for these five AVRs. The comparison along the ridge is highly affected by the distance from the axis surveyed by individual dives. Nevertheless, the AVR at 63.08°N (Area 1) and, to a limited extent, the AVR at 60.24°N (Area 2) are the only places where a sediment cover >90% is observed at less than 1 km from the axis. The estimation of the sediment cover in Area 1 may be influenced by the presence of hydrothermal activity there and the fact that the ROV dives were, in part, aimed at localizing this activity. Close to the Steinaholl vent field, for example, hydrothermal deposits, characterized by their orange ochre color, became much more abundant (J. Taylor et al., 2021), in places completely burying the volcanic landscape. The AVR at 59.27°N (Area 3) has a sediment cover <50% up to ~900 m from the axis, and the AVR at 57.7°N shows the presence of fresh lava flows with a sediment cover <10% up to 3.5 km from the axis.

### 5. Discussion

Plate separation along mid-ocean ridges is accommodated by magmatic and tectonic processes. These processes, which are influenced especially by mantle temperature, magmatic budget, and magma composition, should leave characteristic traces in seafloor morphology. Along the Reykjanes Ridge, variations in crustal thickness away from Iceland (Sinha et al., 1998; Weir et al., 2001; White et al., 1995) suggest that, at first order, the magma



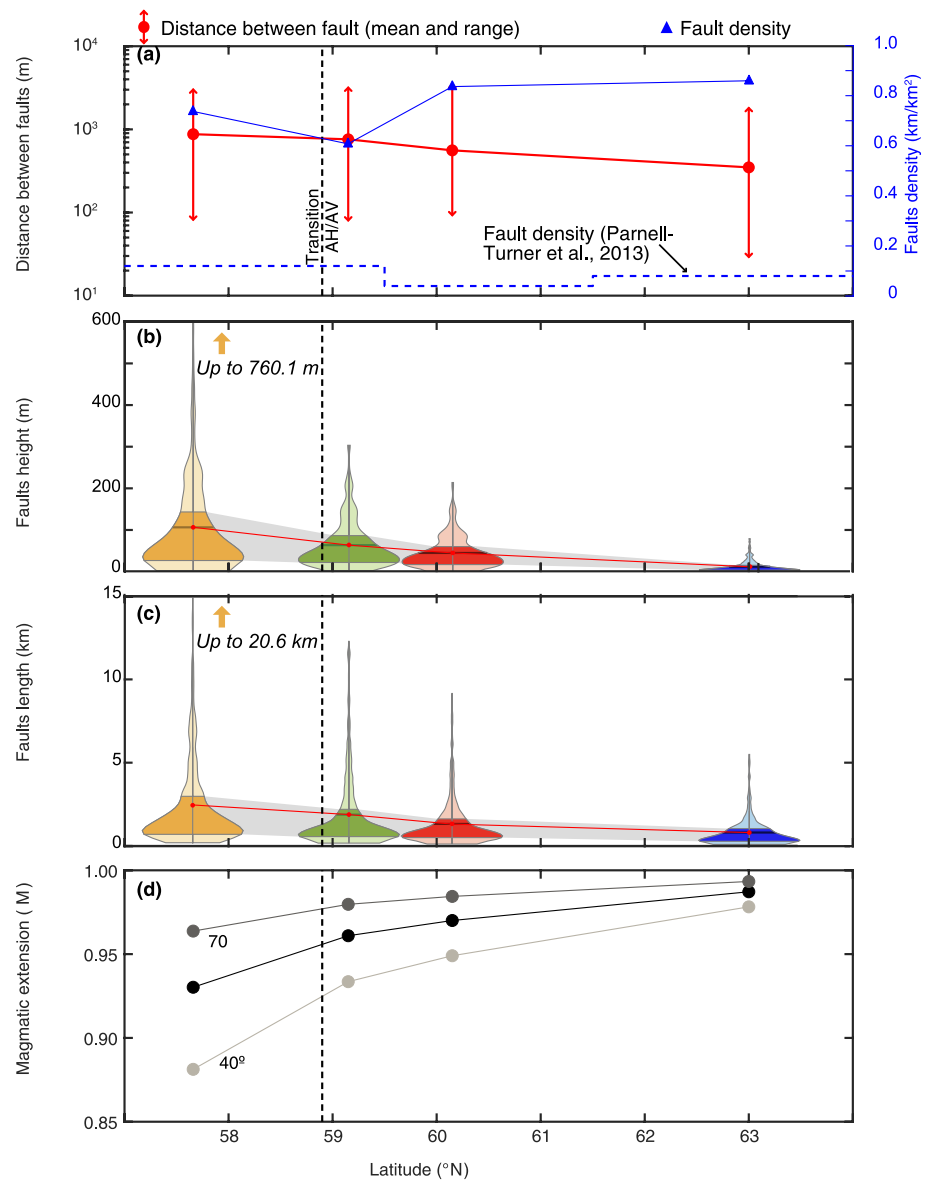


**Figure 4.** Variation of the tectonic pattern and geometry along the axis. (a) Plot of the distance between faults (on the left axis) and fault density by area (on the right axis). The mean distance is indicated by a red dot, and the range by a double arrow. The fault density is shown by a blue triangle. Fault density determined by Parnell-Turner et al. (2013), from 50 m resolution data, is shown by a blue dashed line. (b, c) Violin plot of the fault height (b) fault length (c) by area. The interquartile range (central 50% of the data set in each area) is shown by a darker color, and its along-axis variation is highlighted by the gray background. The red line shows the mean variation along the axis. (d) Along-axis variation of the magmatic extension ( $M$ ). The averages from the individual areas are plotted at their central latitude. The value range by area is indicated by the vertical bars.  $M$  is determined using three different fault angles of 40°, 55°, and 70° based on fault dips measured along the profiles (Figure S3 in Supporting Information S1). The transition from axial high to axial valley is indicated by a vertical dashed line.

supply rate to the axis decreases with increasing distance from Iceland. The across-axis shape of the spreading center also shows variations with distance from Iceland, with the region encompassing our Areas 1, 2 and the northern part of Area 3 being characterized by an axial high morphology (Figures 2 and 3) whereas the region south of ca. 59.1°N, which encompasses part of our Area 3 and all of Area 4, is characterized by the presence of an axial valley. Superimposed on this first-order variation with distance from Iceland are regions of shallower bathymetry, which apparently migrate quite rapidly along-axis, forming “V-shaped ridges.” Our Area 2 lies at the intersection with a VSR (VSR-1 in the nomenclature of Jones et al. (2014)), while Area 3 is clearly south of this

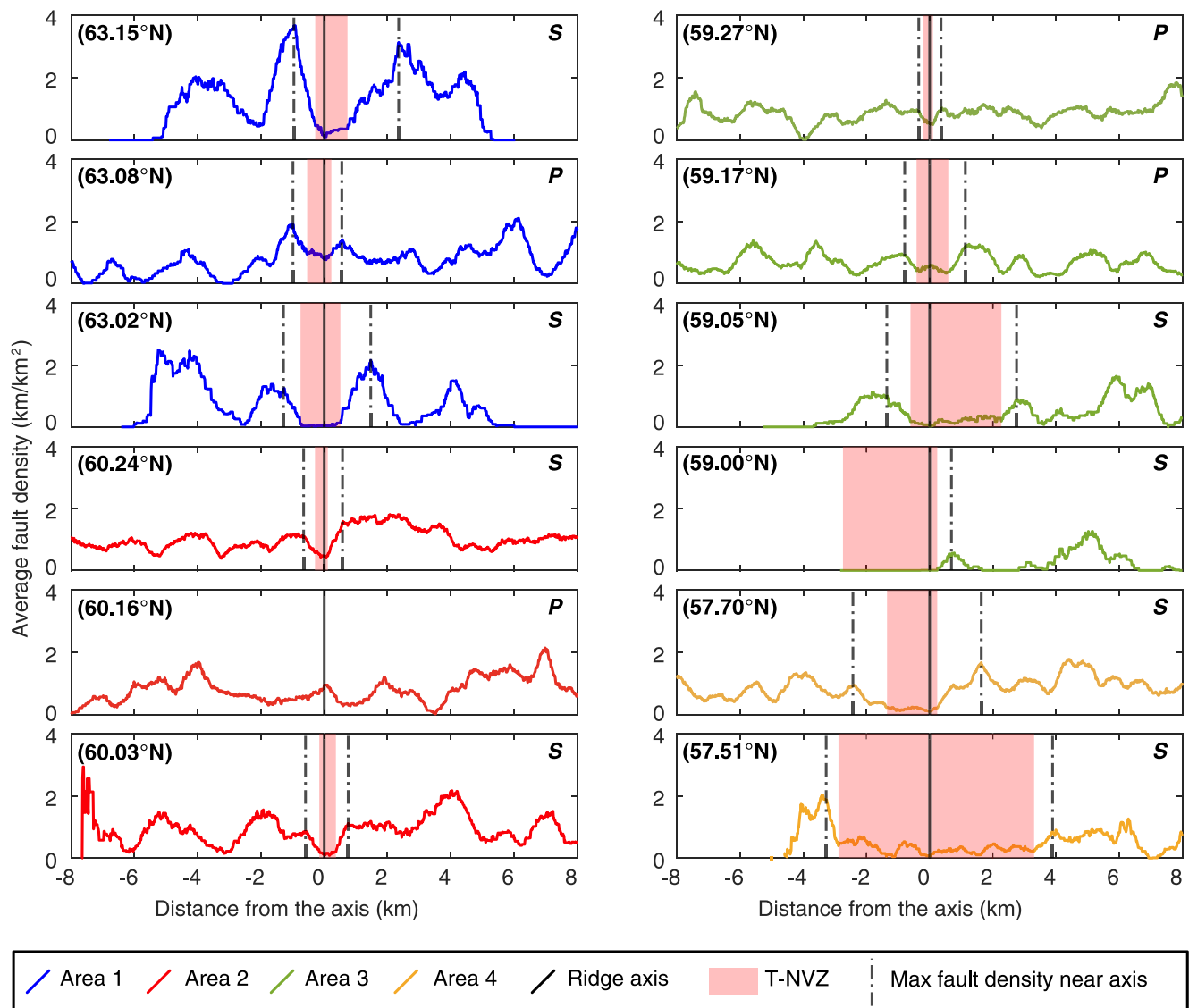


**Figure 5.** Variation of the average fault density across individual Axial Volcanic Ridges (AVRs) from north to south. The profile color corresponds to the area in which the AVR is located, as also used in Figure 4. The AVR axis is indicated by the vertical black line. “P” and “S” in the upper right corner of each bathymetric profile identify AVR with a sharp (S) ridge crest or a plateau (P). The tectonically defined neo-volcanic zone is shaded in pink (see text for definition). The dashed lines locate the points of maximum fault density (“fault density ramps”) in the vicinity of the AVR axis.

intersection (in a region called a “V-shaped trough” by Jones et al., op. cit.) (Figure 7). In the following discussion, we will examine variations in magmatic and tectonic features as a function of distance from Iceland and in relation to the V-shaped ridges, in order to determine their influence on the accretionary processes.

### 5.1. Does Spreading Become More Tectonically Dominated Away From Iceland?

Calculated  $M$  ratios (Behn & Ito, 2008) along the Reykjanes Ridge imply that magmatic extension dominates over tectonic extension ( $M > 0.87$  for all assumed fault dips) along the entire ridge. However,  $M$  decreases with distance from the plume center, with the most rapid change occurring where the axial form changes from a high to a valley (Figure 4d). Although this would seem to clearly imply an increase in tectonic extension away from Iceland, some other complicating factors could be involved:

- *A decrease in sedimentation rates away from Iceland.* The northern section of the Reykjanes Ridge is affected by higher sedimentation rates due to its proximity to the runoff from Iceland (e.g., Ewing & Ewing, 1967; Litvin, 1984). The higher sedimentation rate will cause faults to be more quickly buried and, even if the size

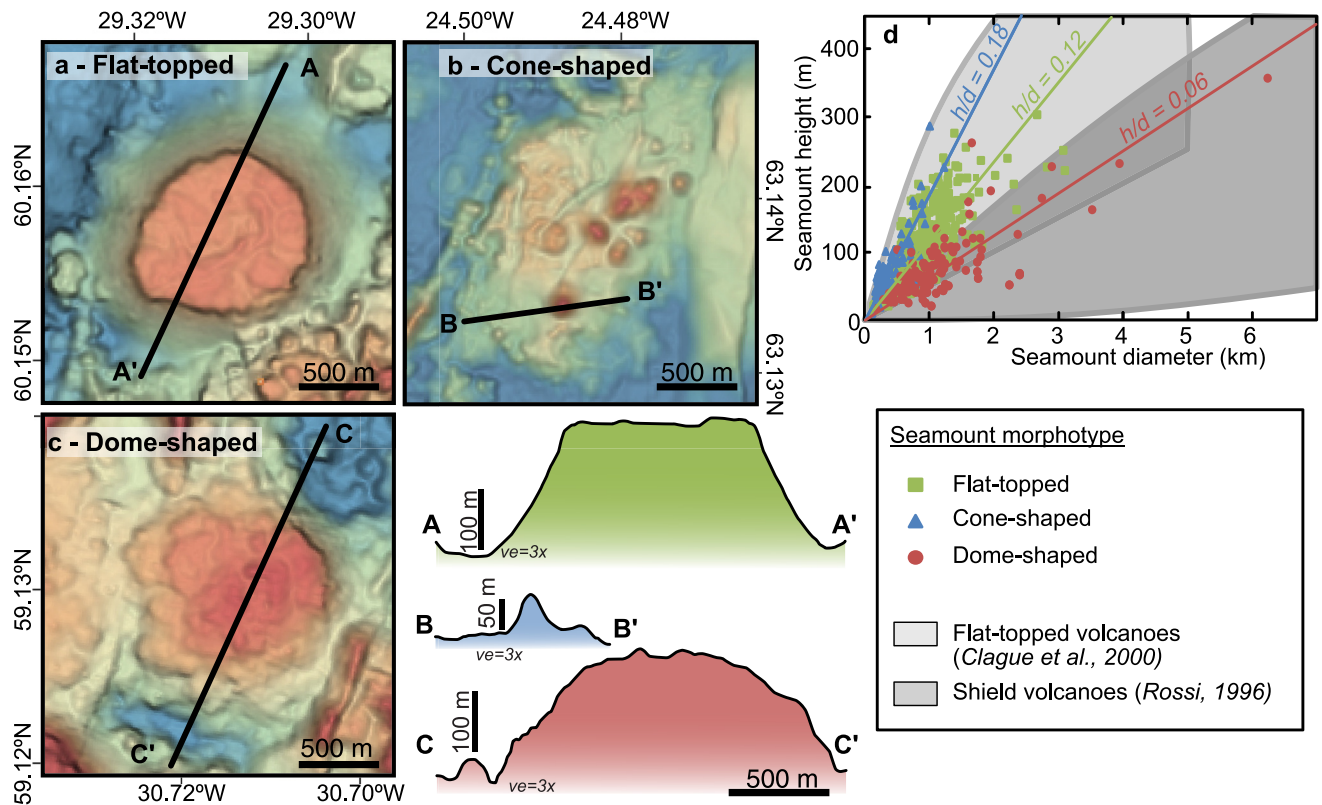


**Figure 6.** (a–c) Detailed bathymetry of individual morphotypes with associated profiles. (a) Flat-topped seamount, (b) Cone-shaped seamount, and (c) Dome-shaped seamount. (d) Height versus diameter diagram of the 571 seamounts measured within the four areas along the Reykjanes Ridge. For comparison, the fields for flat-topped volcanoes (Clague et al., 2000) and shield volcanoes (Rossi, 1996) are shaded with different intensities of gray.

and frequency of faulting were similar along the axis, make faults less apparent in our data near Iceland. This effect is clearly seen in the drop-off in fault density with distance off-axis seen in Area 1 (Figure 5).

- *A bias from the detection limit of the bathymetry data.* As faults are sharp linear steps in bathymetry, their detection is affected by the grid resolution. For very small fault heights, their bathymetric signature becomes so smoothed in the grid as to be undetectable. It is difficult to place quantitative boundaries on this effect, but a fault scarp with a dip of  $55^\circ$  (average measured dip, see Figure S3 in Supporting Information S1) and a height  $<10$  m would be wholly contained in one grid cell at our grid resolution, and so faults with lower heights than this will likely not be detected. This effect is visible in our distribution of fault dips extracted from the grid

**Table 3**  
Seamount Dimension and Distribution by Area

Area name	Surface mapped (km <sup>2</sup> )	Seamount statistics						Seamount morphology distribution <sup>a</sup>		
		Number	Seamount statistics		Individual seamount area (km <sup>2</sup> )	Total seamount area (km <sup>2</sup> )	Surface covered by seamounts (%)	Flat-topped (%)	Dome (%)	Cone (%)
			Diameter (m)	Height (m)						
1	366.31	46	94–3,526	10–197	0.01–9.79	32.4	8.8	56.5	23.9	19.6
2	1,142.02	252	137–2,824	16–302	0.02–6.31	157.4	13.8	70.6	16.3	13.1
3	1,523.20	167	232–3,950	30–286	0.04–9.66	163.0	10.7	60.5	23.4	16.2
4	1,289.32	116	162–6,245	20–36	0.02–30.64	95.1	7.4	51.3	25.2	23.5

<sup>a</sup>Percent based on the number of seamount per area.



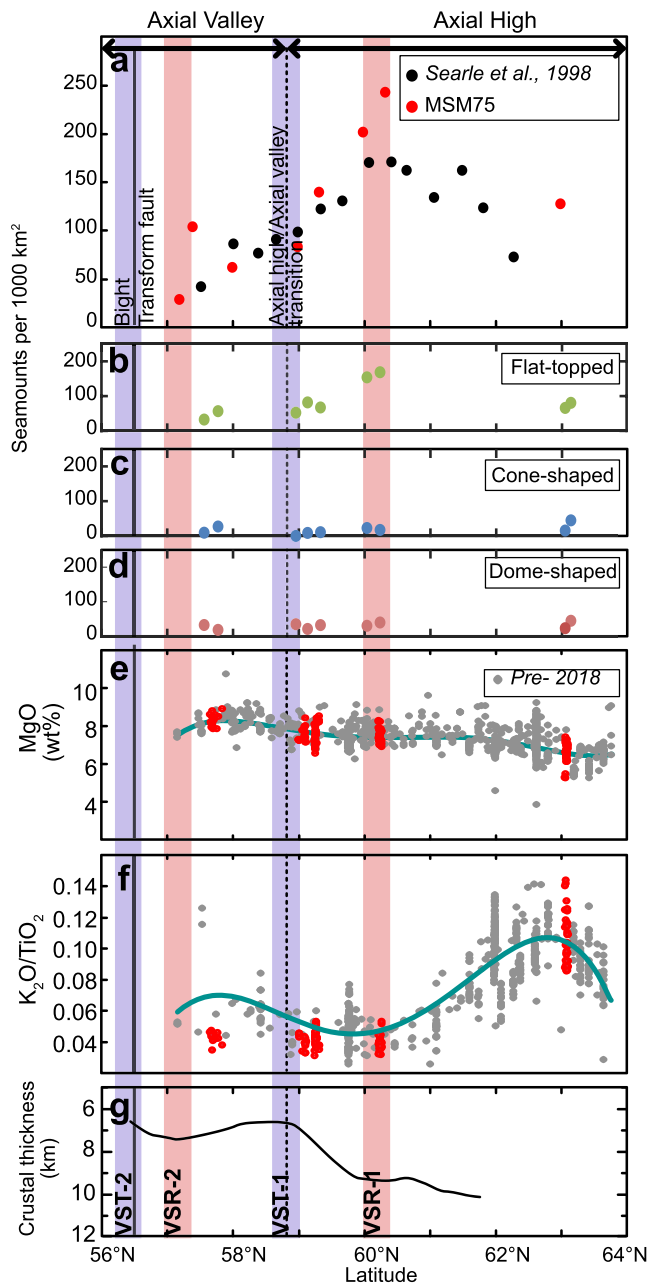


**Figure 7.** Seamount statistics and lava flow chemistry. (a) Plot of the total number of seamounts per 1,000 km<sup>2</sup>. Our data are shown in red, and the data from Searle et al. (1998) in black. (b–d) Plots of the number of flat-topped, cone-shaped, and dome-shaped seamounts per 1,000 km<sup>2</sup> based on our data from the four study areas. (e) Variation of the MgO concentration and (f) K<sub>2</sub>O/TiO<sub>2</sub> ratio along the ridge axis. In plots (e, f), the data from this study are shown in red, and data from the PetDB database ([www.earthchem.org/PetDB](http://www.earthchem.org/PetDB), extracted November 2019) are shown in gray. (g) Plot of the estimated crustal thickness based on wide-angle seismic experiments (modified from Jones et al., 2014). Orange and purple vertical bands locate the intersection of V-shaped ridges (VSR) and V-shaped troughs with the ridge axis, respectively. The vertical dashed line indicates the transition between axial high (in the north) and axial valley (to the south) morphologies.

(Figure S3 in Supporting Information S1). These show a positive correlation with fault height, suggesting that low dips calculated for low fault heights do not reflect the true fault dip but instead the effect of smearing during grid interpolation.

Ground-truth evidence from the ROV dives suggests, however, that neither sedimentation nor bathymetric biases are the dominant factors influencing our fault statistics. In Area 1, we see that even in the essentially unsedimented region close to the axis (see blue bars in Figure 8a), tectonic extension is accommodated by a large number of small faults (in this area, the fault spacing is smallest, while the fault height is lowest, Figures 4a and 4b, respectively). While the fault height observed in Area 2 (1.3–214 m) is similar to those previously evidenced (Parnell-Turner et al., 2013) in this region (~<200 m, Parnell-Turner et al., 2013), our data (Figure 4a) do not show a decrease in fault density in Area 2 as previously observed (Parnell-Turner et al., 2013; Searle et al., 1998), but rather in Area 3. The difference observed in the fault density is most likely the result of the difference in resolution (15 vs. 50 m in Parnell-Turner et al. (2013) and Searle et al. (1998)), as well as the high proportion of faults with a small vertical offset (Figure 4b), probably not found in earlier studies. The most significant change in faulting intensity (reflected by a sharp decrease in *M*) is between Areas 3 and 4, suggesting that processes controlling the axial valley form, rather than the presence or absence of a V-shaped ridge, are important for axial fault development. Ito and Behn (2008) have shown that the development of axial shape is due to what they call the “rise-sink ratio,” related to magmatic accretion and tectonic extension, and so the decrease in *M* seen in Area 4 probably reflects the increasing influence of tectonic processes in this axial valley. We conclude, therefore, that the southward decrease in *M* is related to more tectonically accommodated spreading in the south.

## 5.2. Controls of the Deformation Along the Ridge Axis

As the *M*-ratio decreases, the observed length, height, and spacing of the fault scarps increases with distance from the Iceland plume (Figure 4). This suggests that the way in which extension is accommodated on faults also varies along the ridge. Toward the south, the increase in fault geometry and spacing is consistent with a deepening of the brittle-ductile boundary (Cowie et al., 1993) and a decrease in mantle temperature away from the plume center (Höskuldsson et al., 2007; Parson et al., 1993; Searle et al., 1998; White et al., 1995). Indeed, the brittle-ductile boundary is expected to be shallow near the Reykjanes Peninsula and deepens to reach a depth of ~9 km at 61.6°N and ~15 km at 57.8°N, based on effective elastic thickness estimates (Owens, 1996; Searle et al., 1998). The linear variation in fault geometry and spacing without obvious change at the VSR-ridge intersection (Area 2) indicates that the distance from the plume center is the main parameter controlling the fault geometry. Also, based on these observations, it is unlikely that the VSR results from a thermal pulse (Parnell-Turner et al., 2013, 2017; Poore et al., 2011; Vogt, 1971) as such an anomaly is expected to result in a larger number of small faults.

## 5.3. Cross-Axis Fault Density Variations: A Proxy for the Neovolcanic Zone?

The mean fault density across the axis (Figure 5) shows a fairly consistent pattern at all studied latitudes; low fault densities close to the axis (within

**Table 4**  
*Seamount Geometry by Morphotype*

	Surface (km <sup>3</sup> )		Diameter (m)		Height (m)		$d/h^a$		Slope (°)	
	Range	Mean	Range	Mean	Range	Mean	Range	Mean	Range	Mean
Dome	0.02–30.64	1.39	168–6,245	1,155	16–356	77.4	0.02–0.21	0.08	4.8–24.7	13.7
Flat-topped	0.01–9.66	0.73	130–3,100	886	14–302	108.7	0.05–0.26	0.13	9.1–28.93	18.5
Cone	0.01–1.17	0.16	94–1,220	388	10–286	75.7	0.08–0.39	0.21	13.3–39.9	24.7

<sup>a</sup>Ratio seamount diameter ( $d$ ) over height ( $h$ ).

<3.2 km from the axis), followed by a sharp increase in the fault density (from 0 to 3.7 km/km<sup>2</sup>) over a region which is less than 750 m wide (hereafter called the fault density ramp [FDR]). The outer limit of the FDR is marked by dashed lines in Figure 5. Within the low fault density region between the FDRs, either tectonic deformation of the seafloor is limited (Behn et al., 2006) or the active fault traces are being continually buried by new lava flows, erasing their signature in the bathymetry (Escartín et al., 2007; Le Saout et al., 2018). Our ground-truthing evidence from the ROV dives suggests that the latter is the case, as we see a high proportion of

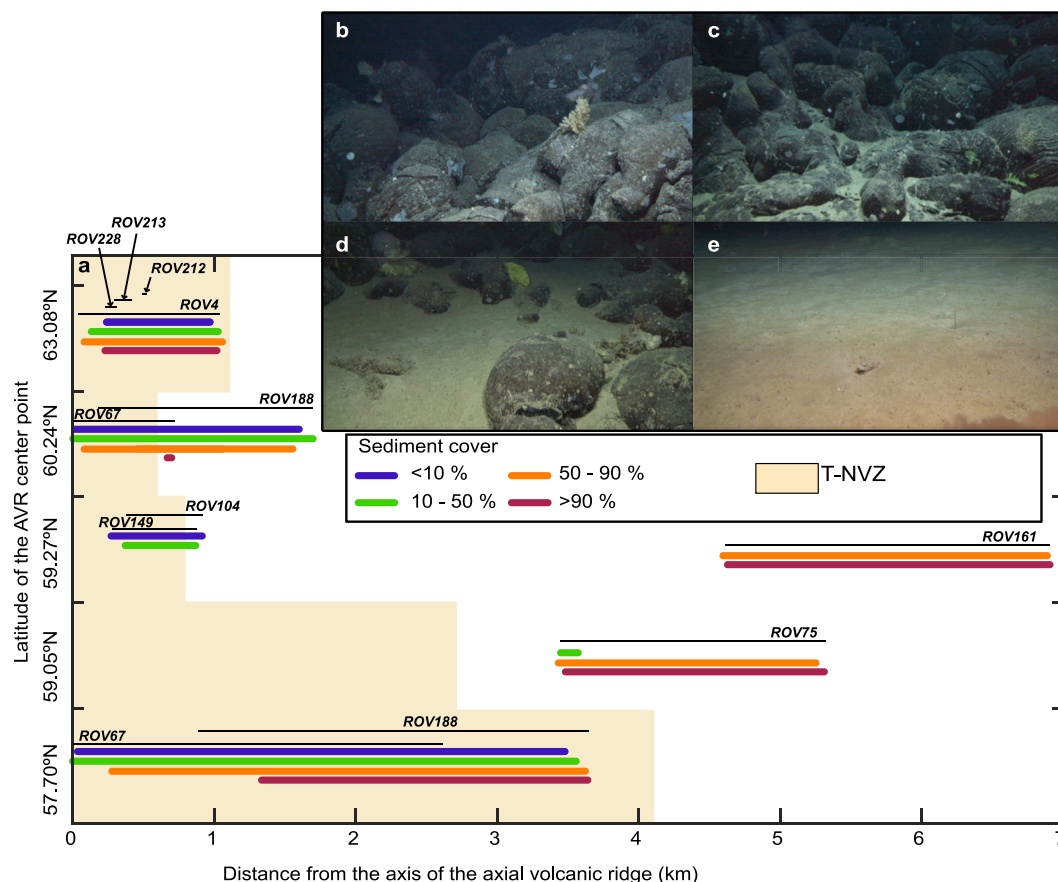


**Figure 8.** (a) Distribution of sediment cover as a function of the distance from the axis for the five Axial Volcanic Ridge (AVR) visually surveyed by the Remotely Operated Vehicle (ROV). The horizontal bars are color-coded according to visual estimations of the percentage of sediment cover determined from the ROV video, using four groups (less 10% in blue, from 10% to 50% in green, from 50% to 90% in orange, and more than 90% in brown). The bars extend from the minimum to the maximum distance from the AVR axis at which one category was observed. The color background shows the maximum extent of the neo-volcanic zone from the axis based on the fault density information shown in Figure 5. Horizontal black lines show the extent of the individual ROV dives. (b–e) Framegrabs from the ROV videos illustrating the different categories of sediment cover. (b) Light dusting on pillows (<10%), (c) some sediment accumulation with isolated sediment pockets (10%–50%), (d) heavy sedimentation with interconnected sediment pockets (50%–90%), and (e) sediment plain (>90%).

fresh-looking lava flows with low sediment cover throughout this region, independent of its width (Figure 8). We then interpret the FDR as marking the boundary of most young eruptive activity and hence of the neovolcanic zone. As this boundary is defined based on fault densities, we refer to the region between the FDRs as the “tectonically defined neo-volcanic zone” (T-NVZ). Of course, the neovolcanic zone can also be defined by the extent of young lava flows observed on the seafloor (for our seafloor observations we used a cut-off at lava flows with less than 10% of sediment cover, see Figure 8), which we then refer to as the “volcanically defined neo-volcanic zone” (V-NVZ). With the exception of Area 2, our study areas show a relatively good correlation between T-NVZ and V-NVZ. However, our observations are limited by where the ROV was deployed.

In Area 2, young, non-sedimented volcanic flows are observed up to 1 km outside the T-NVZ (see Figure 8). Thus, the narrow T-NVZ in this region (<1 km) and generally high axial fault density do not reflect a lack of eruptions. Instead, extrusions most probably occur over a broader region but with limited impact on the average axial fault density. In terms of the style of volcanism, Area 2 is distinguished from the three other sections of the ridge by its higher seamount density and, therefore, higher proportion of point source extrusions (Figure 7a). The presence of numerous unfaulted seamounts away from the T-NVZ confirms that seamount emplacement is not limited to the near-axis region.

#### 5.4. Seamount Type, Distribution, and Their Relationships to V-Shaped Ridges

Seamounts are observed everywhere along the Reykjanes Ridge. However, their density is highly variable and shows clear systematics (Figure 7a). At the southern end of the region, near 57°N, seamount density is 90 seamounts per 1,000 km<sup>2</sup>, similar to the average seamount density observed along the Mid-Atlantic Ridge between 24° and 30°N (~80 per 1,000 km<sup>2</sup>, Smith & Cann, 1992). Seamount density increases rapidly northward, peaking at around 220 seamounts per 1,000 km<sup>2</sup> at 60°N where the VSR intersects the axis. Further north still, the seamount abundance decreases once more, reaching ~125 seamounts per 1,000 km<sup>2</sup> at 64°N. The variation in seamount abundance does not seem to correlate with changes in magma composition, crustal thickness, or the magmatic/tectonic *M* ratio. This observation is in contrast to previous findings at, for example, the Galapagos Spreading Centre where Colman et al. (2012) have shown that seamount density increases as magma budget (and so crustal thickness) decreases.

Most of the variation in seamount density is associated with changes in the proportion of flat-topped volcanoes (Figure 7f). Flat-topped volcanoes can be produced either by a particular combination of eruptive parameters (including magma viscosity, effusion rate, eruption duration, geometry of the feeder-dike, and morphology of the underlying seafloor; see e.g., Bonatti & Harrison, 1988; Clague et al., 2000; Gregg & Fink, 1995) or by post-eruptive erosion of emergent edifices to wave-base (“guyots,” Hess, 1946). There are several considerations which suggest that eruptive rather than erosive processes have generated the flat-topped Reykjanes seamounts: (a) as sea-level has varied by less than ca. 150 m during the Pleistocene (e.g., Waelbroeck et al., 2002), it is unlikely that any areas south of Area 1 would be affected by near-surface planation as the axial seafloor there is deeper than 600 m; (b) adjacent flat-topped seamounts have different summit depths, inconsistent with planation to a common sea-level; and (c) some of the flat-topped seamounts surveyed show clear volcanic structures (e.g., caldera, pressure ridges, tumuli) at their summit, inconsistent with an erosive origin.

Studies elsewhere (Clague et al., 2000) have shown that flat-topped volcanoes are probably monogenetic and that they form at low to moderate effusion rates. On slow-spreading ridges, they are generally found at segment ends and are rare on AVR (Briais et al., 2000). Briais et al. (2000) proposed that they are produced by eruptions sourced directly from the upper mantle, with limited to no storage and differentiation of the magma in a crustal magma chamber.

The peak in seamount abundance, especially flat-topped seamounts, in Area 2 is associated with other distinctive tectonic and magmatic characteristics:

- The mean fault heights (Figure 4e) are low, below those in both Areas 3 and 4, but the fault density (Table 2) is relatively high (0.84 km/km<sup>2</sup> compared to 0.61 and 0.74 in Areas 3 and 4, respectively). This high abundance of small faults in Area 2 suggests that the brittle zone of the crust there is thin, unable to support deep, high-throw faults (Cowie et al., 1994). This is supported by the teleseismic activity (data from 1970 to 2021 available in the [iris.edu](https://iris.lamont.gov/) catalog), which is much lower in Area 2 than in Area 3 or 4 (see Searle et al., 1998 and also Figure 1).



- The NVZ is the narrowest in Area 2, suggesting that large volume, high eruption rate lava flows have not occurred there in recent times.
- Volcanics with <10% sediment cover are found far outside the NVZ, uniquely in Area 2 (Figure 8). This suggests that magmatism is less focused to the axis in this area than in the other areas studied.

Taken together, these disparate lines of evidence suggest that crustal formation in Area 2 is significantly different from that in the other areas and even compared to slow-spreading shallow ridges in general. Thick crust on slow-spreading axes is usually associated with extensive sheet flows and an absence of seamounts and faults (see e.g., Haase et al., 2009), all features suggesting high extrusion rate and/or low viscosity eruptions from a robust crustal magma system. Magmatism in Area 2 seems to take the form of many low-volume batches of magma which either erupt at low rates over a relatively wide cross-axis region building generally flat-topped volcanoes or stall at depth to form a thickened crust. We propose here that this is directly related to another unique feature of Area 2—its location on a VSR. High seamount abundances have previously been observed on two of the few other examples of a VSR known from the world's spreading axes—a V-shaped ridge south of the Azores (Cannat et al., 1999) and north of the Kolbeinsey ridge (Jones et al., 2002; Yeo et al., 2016). Cannat et al. (1999) and Escartín et al. (2001) concluded that the V-shaped ridge south of the Azores is constructed by volcanism occurring over a wide, cross-axis region, leading to excess crustal thicknesses of up to 6 km, and noted that the V-shaped ridge is bathymetrically characterized by an anomalously large number of seamounts covering its summit (most with a diameter of 1–4 km and so directly comparable with those reported here, see Figure 6d).

VSR have been suggested to be caused either by pulses of plume material traveling through the sub-axial mantle (Cannat et al., 1999; Jones et al., 2014; Parnell-Turner et al., 2013, 2017; Poore et al., 2011; Vogt, 1971), propagating rift jumps migrating at crustal levels away from Iceland (Hey et al., 2010) or the passage of a buoyant upwelling melting instability (Martinez & Hey, 2017). The plume pulsing hypothesis is, as Martinez and Hey (2017) point out, difficult to reconcile with the angle between the VSR and the trend of the Reykjanes Ridge which require the causative melting anomaly to migrate at almost 170 mm/yr (Ito, 2001), much faster than any feasible plume flow velocities. The difference between the volcanic features we observe in Area 2 and those seen at other plume-influenced ridges (e.g., Galapagos, Colman et al., 2012; Southern MAR, Haase et al., 2009) adds weight to the conclusion that plume material is not the cause of the VSR, as in this case we would expect an increase in large sheet and lobate flows and a decrease in the incidence of flat-topped volcanoes, exactly opposite to our observations. The idea of propagating rift jumps can also be excluded by our data as they should be associated with anomalously high fault densities at the axis, a feature not seen in Area 2. Instead, the observational evidence for a fusible mantle producing many small magma batches over quite a wide cross-axis region appears most compatible with the buoyant upwelling melting instability proposal. Such a buoyant upwelling zone, which operates in addition to the passive mantle upwelling associated with plate separation, may allow a significant proportion of melts to escape from the corner-flow focusing of magma to the axis (Figure 9). As a consequence, numerous small magma batches would enter the crust over an area wider than the T-NVZ.

The extended cross-axis distribution of magma could allow a thick crust to be generated without producing a permanent axial magma chamber. Without a magma chamber, the individual batches either erupt (forming flat-topped volcanoes of relatively small volume) or cool in the crust (building the thick lower crust characteristic of thickened crust) as multiple sills. The idea that Area 2 is not underlain by a permanent magma chamber is confirmed by seismic studies (Parnell-Turner et al., 2013) and is also supported by the magmatic MgO contents. At 8%, these are similar to slow-spreading ridges elsewhere and higher than magmas from the shallow Lilliput region of the Southern Mid-Atlantic Ridge (e.g., Haase et al., 2009) or the East-Pacific Rise where fractionation in a magma chamber leads to an average MgO around 6% (Rubin et al., 2009). Figure 9 summarizes our observations and presents a model for the crust and upper mantle architecture based on the buoyant upwelling mantle model of Martinez et al. (2019).

## 6. Conclusion

Our detailed mapping and ground-truthing observations allow us to make some general statements about the relationship between tectonism and volcanism on the Reykjanes Ridge:

1. The extension along the Reykjanes Ridge is primarily accommodated through magmatic activity. However, the variation of horizontal displacement along fault scarps shows an increase in the proportion of the deformation

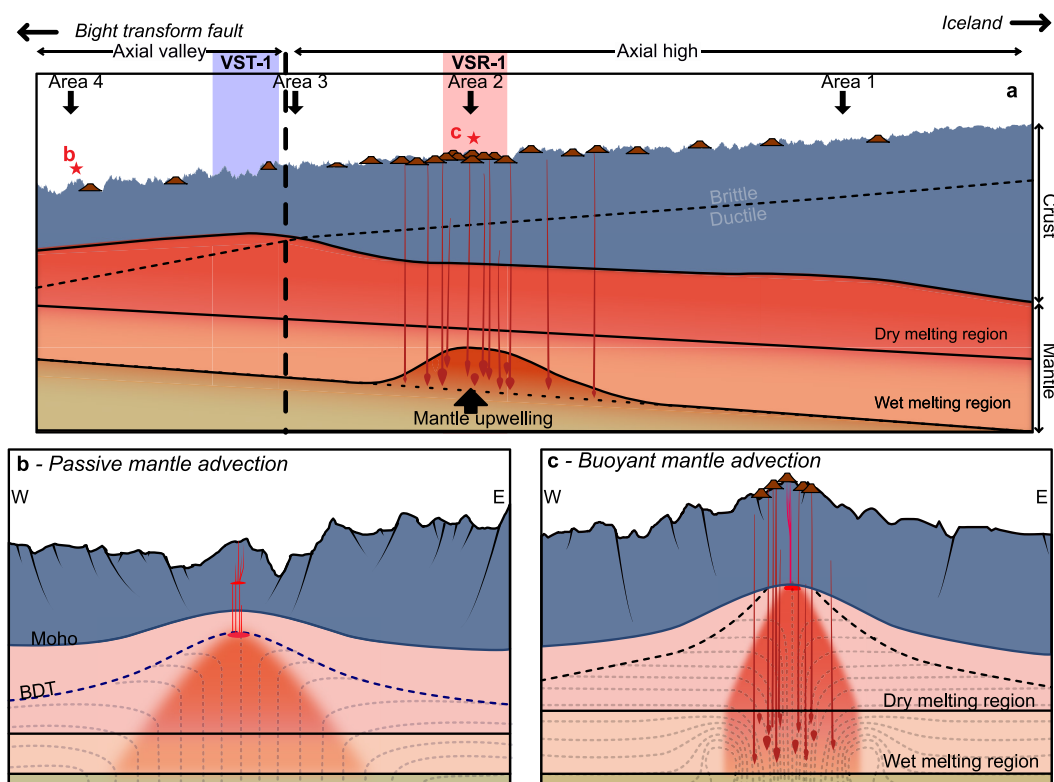


**Figure 9.** Conceptual models illustrating the relationship between mantle, crustal properties, and eruptive activity along and across the Reykjanes Ridge axis associated with the propagation of a buoyant mantle upwelling. Adapted, with additions, from Martinez et al. (2019) (a) Along axis variations, from 57°N to the Reykjanes peninsula. The V-shaped ridges (pink) and V-shaped troughs (blue) are highlighted by a color background. The brittle/ductile transition (black dashed line) depth is based on the estimation of the effective elastic thickness (Owens, 1996; Searle et al., 1998). The location of the four study areas is indicated by downward arrows, and the cross-sections (b, c) are indicated by red stars. (b, c) Bathymetric cross-sections showing mantle melting zone and flowlines (dashed gray lines) associated with (b) a passive mantle advection and (c) a buoyant mantle advection. The axial zone of melt accumulation and axial dike intrusions are indicated in red. The deep melt pockets from the mantle upwelling and the resulting flat-topped seamounts are indicated in brown on the three figures.

- accommodated by tectonic activity toward the south, with an increase at the transition between axial high and axial valley.
- With distance from Iceland, the mean fault height, length, and spacing within 10 km of the axis increase systematically. This is probably the result of an increasingly brittle crust being able to support larger-throw faults. Our result suggests that the decrease in mantle temperature away from the plume is the primary factor controlling the regional fault pattern and geometry.
- At the ridge axis, a region of low fault density delimits a tectonically defined neovolcanic zone, probably the result of many faults being buried by younger lava flows. The neovolcanic zone is bounded to both sides by a steep increase in fault density (fault density ramp). Only Area 2 shows a decoupling between the neovolcanic zone defined by fault density or sediment thickness as a result of seamount emplacement over a wider region.
- The seamount abundance varies strongly and systematically along axis but is not correlated with magma chemistry. Highest seamount abundances (dominated by flat-topped seamount) occur where a regional V-shaped ridge intersects the axis. The thick crust at this intersection appears to be constructed from many small-volume magma batches intruding or erupting over a wide cross-axis region. This is most compatible with the V-shaped ridge being generated by a buoyant upwelling melting anomaly propagating through the sub-axial mantle as has been recently proposed based on geophysical data.

## Conflict of Interest

The authors declare no conflicts of interest relevant to this study.

## Data Availability Statement

The multibeam bathymetric data used in the study, and the detailed analyses of the MSM75 rock and glass samples are publicly available on the PANGAEA repository (<https://doi.org/10.1594/PANGAEA.922925> and <https://doi.org/10.1594/PANGAEA.956077>, respectively).

## Acknowledgments

We thank Capt. Björn Maaß and his crew, together with the GEOMAR ROV team for their excellent support in acquiring the data presented here. We thank the anonymous reviewers whose comments and questions allowed us to improve this manuscript. The MSM75 cruise was financially supported by the German Science Foundation (DFG) and the Helmholtz Association (via core funding to GEOMAR).

## References

- Appelgate, B., & Shor, A. N. (1994). The northern mid-Atlantic and Reykjanes Ridges: Spreading center morphology between 55°50'N and 63°00'N. *Journal of Geophysical Research*, 99(B9), 17935–17956. <https://doi.org/10.1029/93jb03459>
- Argus, D. F., Gordon, R. G., & DeMets, C. (2011). Geologically current motion of 56 plates relative to the no-net-rotation reference frame. *Geochemistry, Geophysics, Geosystems*, 12(11), Q11001. <https://doi.org/10.1029/2011gc003751>
- Augustin, N., van der Zwan, F. M., Devey, C. W., Ligi, M., Kwasnitschka, T., Feldens, P., et al. (2016). Geomorphology of the central Red Sea Rift: Determining spreading processes. *Geomorphology*, 274, 162–179. <https://doi.org/10.1016/j.geomorph.2016.08.028>
- Behn, M. D., Buck, R. W., & Sacks, S. I. (2006). Topographic controls on dike injection in volcanic rift zones. *Earth and Planetary Science Letters*, 246(3–4), 188–196. <https://doi.org/10.1016/j.epsl.2006.04.005>
- Behn, M. D., & Ito, G. (2008). Magmatic and tectonic extension at mid-ocean ridges: 1. Controls on fault characteristics. *Geochemistry, Geophysics, Geosystems*, 9(8), Q08O10. <https://doi.org/10.1029/2008gc001965>
- Bonatti, E., & Harrison, C. G. A. (1988). Eruption styles of basalt in oceanic spreading ridges and seamounts: Effect of magma temperature and viscosity. *Journal of Geophysical Research*, 93(B4), 2967–2980. <https://doi.org/10.1029/JB093iB04p02967>
- Briais, A., Sloan, H., Parson, L. M., & Murton, B. J. (2000). Accretionary processes in the axial valley of the Mid-Atlantic Ridge 27°N–30°N from TOBI side-scan sonar images. *Marine Geophysical Researches*, 21(1–2), 87–119. <https://doi.org/10.1023/a:1004722213652>
- Brix, S., Taylor, J., Le Saout, M., Mercado-Salas, N., Kaiser, S., Lörz, A.-N., et al. (2020). Depth transects and connectivity along gradients in the North Atlantic and Nordic Seas in the frame of the IceAGE project (Icelandic marine animals: Genetics and ecology). Cruise No. S0276 (MerMet17-06), 22.06.2020 – 26.07.2020, Emden (Germany) – Emden (Germany). SONNE-Berichte, Gutachterpanel Forschungsschiffe (p. 48). [https://doi.org/10.48433/cr\\_so276](https://doi.org/10.48433/cr_so276)
- Cannat, M., Briais, A., Deplus, C., Escartín, J., Georgen, J., Lin, J., et al. (1999). Mid-Atlantic Ridge–Azores hotspot interactions: Along-axis migration of a hotspot-derived event of enhanced magmatism 10 to 4 Ma ago. *Earth and Planetary Science Letters*, 173(3), 257–269. [https://doi.org/10.1016/S0012-821X\(99\)00234-4](https://doi.org/10.1016/S0012-821X(99)00234-4)
- Carbotte, S. M., Ryan, W. B. F., Jin, W., Cormier, M., Bergmanis, E., Sinton, J., & White, S. (2003). Magmatic subsidence of the East Pacific Rise (EPR) at 18°14'S revealed through fault restoration of ridge crest bathymetry. *Geochemistry, Geophysics, Geosystems*, 4(1), 1008. <https://doi.org/10.1029/2002gc000337>
- Clague, D. A., Moore, J. G., & Reynolds, J. R. (2000). Formation of submarine flat-topped volcanic cones in Hawai'i. *Bulletin of Volcanology*, 62(3), 214–233. <https://doi.org/10.1007/s004450000088>
- Colman, A., Sinton, J. M., White, S. M., McClinton, T. J., Bowles, J. A., Rubin, K. H., et al. (2012). Effects of variable magma supply on mid-ocean ridge eruptions: Constraints from mapped lava flow fields along the Galápagos Spreading Center. *Geochemistry, Geophysics, Geosystems*, 13(8), Q08014. <https://doi.org/10.1029/2012GC004163>
- Cowie, P. A., Malinverno, A., Ryan, W. B. F., & Edwards, M. H. (1994). Quantitative fault studies on the East Pacific Rise: A comparison of sonar imaging techniques. *Journal of Geophysical Research*, 99(B8), 15205–15218. <https://doi.org/10.1029/94jb00041>
- Cowie, P. A., Scholz, C. H., Edwards, M., & Malinverno, A. (1993). Fault strain and seismic coupling on mid-ocean ridges. *Journal of Geophysical Research*, 98(B10), 17911–17920. <https://doi.org/10.1029/93JB01567>
- DeMets, C., Gordon, R. G., Argus, D. F., & Stein, S. (1994). Effect of recent revisions to the geomagnetic reversal time scale on estimates of current plate motions. *Geophysical Research Letters*, 21(20), 2191–2194. <https://doi.org/10.1029/94gl02118>
- Detrick, R., Sinton, J., Ito, G., Canales, J., Behn, M., Blacic, T., et al. (2002). Correlated geophysical, geochemical, and volcanological manifestations of plume-ridge interaction along the Galápagos Spreading Center. *Geochemistry, Geophysics, Geosystems*, 3(10), 1–14. <https://doi.org/10.1029/2002GC000350>
- Devey, C. W., Brix, S., Barua, A., Bodendorfer, M., Cuno, P., Frutos, I., et al. (2022). Detailed mapping and sampling of the Reykjanes Ridge, Cruise No. MSM75, 29.06.2018 – 08.08.2018, Reykjavik (Iceland) – Reykjavik (Iceland). In *MARIA S. MERIAN-Berichte* (p. 89). Begutachtungspanel Forschungsschiffe. MSM75. [https://doi.org/10.48433/cr\\_msm75](https://doi.org/10.48433/cr_msm75)
- Devey, C. W., & Le Saout, M. (2023). Major element composition of glass samples from Maria S. Merian cruise MSM75 along the Reykjanes Ridge [Dataset]. PANGAEA. <https://doi.org/10.1594/PANGAEA.956077>
- Devey, C. W., Le Saout, M., Petersen, S., Palgan, D., Tomkowicz, A., von Bosse, T., & Wölfl, A.-C. (2020). *Multibeam bathymetry raw data (Kongsberg EM 712 entire dataset) of RV MARIA S. MERIAN during cruise MSM75*. GEOMAR – Helmholtz Centre for Ocean Research Kiel. <https://doi.org/10.1594/PANGAEA.922925>
- Escartín, J., Cannat, M., Pouliquen, G., Rabain, A., & Lin, J. (2001). Crustal thickness of V-shaped ridges south of the Azores: Interaction of the Mid-Atlantic Ridge (36°–39°N) and the Azores hot spot. *Journal of Geophysical Research: Solid Earth*, 106(B10), 21719–21735. <https://doi.org/10.1029/2001JB000224>
- Escartín, J., Soule, S., Fornari, D., Tivey, M., Schouten, H., & Perfit, M. (2007). Interplay between faults and lava flows in construction of the upper oceanic crust: The East Pacific Rise crest 9°25'–9°58'N. *Geochemistry, Geophysics, Geosystems*, 8(6), Q06005. <https://doi.org/10.1029/2006GC001399>
- Ewing, J., & Ewing, M. (1967). Sediment distribution on the mid-ocean ridges with respect to spreading of the sea floor. *Science*, 156(3782), 1590–1592. <https://doi.org/10.1126/science.156.3782.1590>
- German, C. R., Briem, J., Chin, C., Danielsen, M., Holland, S., James, R., et al. (1994). Hydrothermal activity on the Reykjanes Ridge: The Steinahóll vent-field at 63°06'N. *Earth and Planetary Science Letters*, 121(3–4), 647–654. [https://doi.org/10.1016/0012-821X\(94\)90098-1](https://doi.org/10.1016/0012-821X(94)90098-1)



- Gregg, T. K., & Fink, J. H. (1995). Quantification of submarine lava-flow morphology through analog experiments. *Geology*, 23(1), 73–76. [https://doi.org/10.1130/0091-7613\(1995\)023<0073:QOSLFM>2.3.CO;2](https://doi.org/10.1130/0091-7613(1995)023<0073:QOSLFM>2.3.CO;2)
- Haase, K. M., Koschinsky, A., Petersen, S., Devey, C. W., German, C., Lackschewitz, K. S., et al. (2009). Diking, young volcanism and diffuse hydrothermal activity on the southern Mid-Atlantic Ridge: The Lilliput field at 9°33'S. *Marine Geology*, 266(1–4), 52–64. <https://doi.org/10.1016/j.margeo.2009.07.012>
- Hanan, B. B., Blichert-Toft, J., Kingsley, R., & Schilling, J.-G. (2000). Depleted Iceland mantle plume geochemical signature: Artifact of multi-component mixing? *Geochemistry, Geophysics, Geosystems*, 1(4), 1003. <https://doi.org/10.1029/1999gc000009>
- Hanan, B. B., Kingsley, R. H., & Schilling, J.-G. (1986). Pb isotope evidence in the south Atlantic for migrating ridge—Hotspot interactions. *Nature*, 322(6075), 137–144. <https://doi.org/10.1038/322137a0>
- Hart, S. R., Schilling, J.-G., & Powell, J. L. (1973). Basalts from Iceland and along the Reykjanes Ridge: Sr isotope geochemistry. *Nature Physical Science*, 246(155), 104–107. <https://doi.org/10.1038/physci246104a0>
- Hess, H. H. (1946). Drowned ancient islands of the Pacific Basin. *Eos, Transactions American Geophysical Union*, 27(6), 875. <https://doi.org/10.1029/tr027i006p00875>
- Hey, R., Martinez, F., Höskuldsson, Á., & Benediktsdóttir, Á. (2010). Propagating rift model for the V-shaped ridges south of Iceland. *Geochemistry, Geophysics, Geosystems*, 11(3), Q03011. <https://doi.org/10.1029/2009gc002865>
- Höskuldsson, Á., Hey, R., Kjartansson, E., & Guðmundsson, G. B. (2007). The Reykjanes Ridge between 63°10'N and Iceland. *Journal of Geodynamics*, 43(1), 73–86. <https://doi.org/10.1016/j.jog.2006.09.003>
- Howell, S. M., Ito, G., Behn, M. D., Martinez, F., Olive, J., & Escartin, J. (2016). Magmatic and tectonic extension at the Chile Ridge: Evidence for mantle controls on ridge segmentation. *Geochemistry, Geophysics, Geosystems*, 17(6), 2354–2373. <https://doi.org/10.1002/2016gc006380>
- Ito, G. (2001). Reykjanes 'V'-shaped ridges originating from a pulsing and dehydrating mantle plume. *Nature*, 411(6838), 681–684. <https://doi.org/10.1038/35079561>
- Ito, G., & Behn, M. D. (2008). Magmatic and tectonic extension at mid-ocean ridges: 2. Origin of axial morphology. *Geochemistry, Geophysics, Geosystems*, 9(9), Q09O12. <https://doi.org/10.1029/2008GC001970>
- Ito, G., & Lin, J. (1995). Oceanic spreading center—hotspot interactions: Constraints from along-isochron bathymetric and gravity anomalies. *Geology*, 23(7), 657–660. [https://doi.org/10.1130/0091-7613\(1995\)023<0657:oschic>2.3.co;2](https://doi.org/10.1130/0091-7613(1995)023<0657:oschic>2.3.co;2)
- Ito, G., Lin, J., & Graham, D. (2003). Observational and theoretical studies of the dynamics of mantle plume—mid-ocean ridge interaction. *Reviews of Geophysics*, 41(4), 1017. <https://doi.org/10.1029/2002RG000117>
- Jarosewich, E. (2002). Smithsonian microbeam standards. *Journal of Research of the National Institute of Standards and Technology*, 107(6), 681–685. <https://doi.org/10.6028/jres.107.054>
- Jones, S. M., Murton, B. J., Fitton, J. G., White, N. J., MacLennan, J., & Walters, R. L. (2014). A joint geochemical–geophysical record of time-dependent mantle convection south of Iceland. *Earth and Planetary Science Letters*, 386, 86–97. <https://doi.org/10.1016/j.epsl.2013.09.029>
- Jones, S. M., White, N., & MacLennan, J. (2002). V-shaped ridges around Iceland: Implications for spatial and temporal patterns of mantle convection. *Geochemistry, Geophysics, Geosystems*, 3(10), 1–23. <https://doi.org/10.1029/2002gc000361>
- Keeton, J. A., Searle, R. C., Peirce, C., Parsons, B., White, R. S., Sinha, M. C., et al. (1997). Bathymetry of the Reykjanes Ridge. *Marine Geophysical Researches*, 19(1), 55–64. <https://doi.org/10.1023/a:1004266721393>
- Keller, R. A., Fisk, M. R., & White, W. M. (2000). Isotopic evidence for Late Cretaceous plume–ridge interaction at the Hawaiian hotspot. *Nature*, 405(6787), 673–676. <https://doi.org/10.1038/35015057>
- Le Saout, M., Thibaud, R., & Gente, P. (2018). Detailed analysis of near tectonic features along the East Pacific rise at 16°N, near the mathematician hot spot. *Journal of Geophysical Research: Solid Earth*, 123(6), 4478–4499. <https://doi.org/10.1029/2017jb015301>
- Litvin, V. M. (1984). The morphostructure of the Atlantic Ocean floor. *Its Development in the Meso-Cenozoic*, 127–154. [https://doi.org/10.1007/978-94-009-6245-3\\_6](https://doi.org/10.1007/978-94-009-6245-3_6)
- Magde, L. S., & Smith, D. K. (1995). Seamount volcanism at the Reykjanes Ridge: Relationship to the Iceland hot spot. *Journal of Geophysical Research*, 100(B5), 8449–8468. <https://doi.org/10.1029/95jb00048>
- Martinez, F., & Hey, R. (2017). Propagating buoyant mantle upwelling on the Reykjanes Ridge. *Earth and Planetary Science Letters*, 457, 10–22. <https://doi.org/10.1016/j.epsl.2016.09.057>
- Martinez, F., Hey, R., & Höskuldsson, Á. (2019). Reykjanes Ridge evolution: Effects of plate kinematics, small-scale upper mantle convection and a regional mantle gradient. *Earth-Science Reviews*, 206, 102956. <https://doi.org/10.1016/j.earscirev.2019.102956>
- McClinton, T., White, S. M., Colman, A., & Sinton, J. M. (2013). Reconstructing lava flow emplacement processes at the hot spot-affected Galápagos Spreading Center, 95°W and 92°W. *Geochemistry, Geophysics, Geosystems*, 14(8), 2731–2756. <https://doi.org/10.1002/ggge.20157>
- Murton, B. J., & Parson, L. M. (1993). Segmentation, volcanism and deformation of oblique spreading centres: A quantitative study of the Reykjanes Ridge. *Tectonophysics*, 222(2), 237–257. [https://doi.org/10.1016/0040-1951\(93\)90051-k](https://doi.org/10.1016/0040-1951(93)90051-k)
- Murton, B. J., Taylor, R. N., & Thirlwall, M. F. (2002). Plume–Ridge interaction: A geochemical perspective from the Reykjanes Ridge. *Journal of Petrology*, 43(11), 1987–2012. <https://doi.org/10.1093/petrology/43.11.1987>
- Nadin, P. A., Kusznir, N. J., & Toth, J. (1995). Transient regional uplift in the early tertiary of the northern north Sea and the development of the Iceland plume. *Journal of the Geological Society*, 152(6), 953–958. <https://doi.org/10.1144/gsl.jgs.1995.152.01.12>
- Owens, R. (1996). *The morphology and tectonics of the Reykjanes Ridge*, Doctoral dissertation. University of Oxford.
- Patgan, D., Devey, C. W., & Yeo, I. A. (2017). Volcanism and hydrothermalism on a hotspot-influenced ridge: Comparing Reykjanes Peninsula and Reykjanes Ridge, Iceland. *Journal of Volcanology and Geothermal Research*, 348, 62–81. <https://doi.org/10.1016/j.jvolgeores.2017.10.017>
- Parnell-Turner, R., White, N., Henstock, T. J., Jones, S. M., MacLennan, J., & Murton, B. J. (2017). Causes and consequences of diachronous V-shaped ridges in the north Atlantic Ocean. *Journal of Geophysical Research: Solid Earth*, 122(11), 8675–8708. <https://doi.org/10.1002/2017jb014225>
- Parnell-Turner, R. E., White, N. J., MacLennan, J., Henstock, T. J., Murton, B. J., & Jones, S. M. (2013). Crustal manifestations of a hot transient pulse at 60°N beneath the Mid-Atlantic Ridge. *Earth and Planetary Science Letters*, 363, 109–120. <https://doi.org/10.1016/j.epsl.2012.12.030>
- Parson, L., Murton, B., Searle, R., Booth, D., Evans, J., Field, P., et al. (1993). En echelon axial volcanic ridges at the Reykjanes Ridge: A life cycle of volcanism and tectonics. *Earth and Planetary Science Letters*, 117(1–2), 73–87. [https://doi.org/10.1016/0012-821X\(93\)90118-S](https://doi.org/10.1016/0012-821X(93)90118-S)
- Poore, H., White, N., & MacLennan, J. (2011). Ocean circulation and mantle melting controlled by radial flow of hot pulses in the Iceland plume. *Nature Geoscience*, 4(8), 558–561. <https://doi.org/10.1038/ngeo1161>
- Richards, M. A., Hager, B. H., & Sleep, N. H. (1988). Dynamically supported geoid highs over hotspots: Observation and theory. *Journal of Geophysical Research*, 93(B7), 7690–7708. <https://doi.org/10.1029/jb093ib07p07690>
- Rossi, M. J. (1996). Morphology and mechanism of eruption of postglacial shield volcanoes in Iceland. *Bulletin of Volcanology*, 57(7), 530–540. <https://doi.org/10.1007/BF00304437>
- Rubin, K. H., Sinton, J. M., MacLennan, J., & Hellebrand, E. (2009). Magmatic filtering of mantle compositions at mid-ocean-ridge volcanoes. *Nature Geoscience*, 2(5), 321–328. <https://doi.org/10.1038/ngeo504>

- Sæmundsson, K. (1979). Outline of the geology of Iceland. *Jökull Journal*, 29(1), 7–28. <https://doi.org/10.33799/jokull1979.29.007>
- Schilling, J.-G. (1973a). Iceland Mantle plume. *Nature*, 246(5429), 141–143. <https://doi.org/10.1038/246141a0>
- Schilling, J.-G. (1973b). Iceland Mantle plume: Geochemical study of Reykjanes Ridge. *Nature*, 242(5400), 565–571. <https://doi.org/10.1038/242565a0>
- Schilling, J.-G., Zajac, M., Evans, R., Johnston, T., White, W., Devine, J. D., & Kingsley, R. (1983). Petrologic and geochemical variations along the Mid-Atlantic Ridge from 29 degrees N to 73 degrees N. *American Journal of Science*, 283(6), 510–586. <https://doi.org/10.2475/ajs.283.6.510>
- Searle, R. C., Keeton, J. A., Owens, R. B., White, R. S., Mecklenburgh, R., Parsons, B., & Lee, S. M. (1998). The Reykjanes Ridge: Structure and tectonics of a hot-spot-influenced, slow-spreading ridge, from multibeam bathymetry, gravity and magnetic investigations. *Earth and Planetary Science Letters*, 160(3–4), 463–478. [https://doi.org/10.1016/s0012-821x\(98\)00104-6](https://doi.org/10.1016/s0012-821x(98)00104-6)
- Searle, R. C., & Laughton, A. S. (1981). Fine-scale sonar study of tectonics and volcanism on the Reykjanes Ridge. *Oceanologica Acta, Special issue*.
- Sinha, M. C., Constable, S. C., Peirce, C., White, A., Heinson, G., MacGregor, L. M., & Navin, D. A. (1998). Magmatic processes at slow spreading ridges: Implications of the RAMESSES experiment at 57°45'N on the Mid-Atlantic Ridge. *Geophysical Journal International*, 135(3), 731–745. <https://doi.org/10.1046/j.1365-246x.1998.00704.x>
- Sinton, J., Detrick, R., Canales, P. J., Ito, G., & Behn, M. (2003). Morphology and segmentation of the western Galápagos Spreading Center, 90.5°–98°W: Plume-ridge interaction at an intermediate spreading ridge. *Geochemistry, Geophysics, Geosystems*, 4(12), 8515. <https://doi.org/10.1029/2003GC000609>
- Smallwood, J. R., & White, R. S. (1998). Crustal accretion at the Reykjanes Ridge, 61°–62°N. *Journal of Geophysical Research*, 103(B3), 5185–5201. <https://doi.org/10.1029/97jb03387>
- Smith, D. K., & Cann, J. R. (1992). The role of seamount volcanism in crustal construction at the Mid-Atlantic Ridge (24°–30°N). *Journal of Geophysical Research*, 97(B2), 1645–1658. <https://doi.org/10.1029/91jb02507>
- Sun, S.-S., Tatsumoto, M., & Schilling, J.-G. (1975). Mantle plume mixing along the Reykjanes Ridge axis: Lead isotopic evidence. *Science*, 190(4210), 143–147. <https://doi.org/10.1126/science.190.4210.143>
- Talwani, M., Windisch, C. C., & Langseth, M. G. (1971). Reykjanes Ridge crest: A detailed geophysical study. *Journal of Geophysical Research*, 76(2), 473–517. <https://doi.org/10.1029/jb076i002p00473>
- Taylor, J., Devey, C., Saout, M. L., Petersen, S., Kwasnitschka, T., Frutos, I., et al. (2021). The discovery and preliminary geological and faunal descriptions of three new Steinahóll vent sites, Reykjanes Ridge, Iceland. *Frontiers in Marine Science*, 8, 520713. <https://doi.org/10.3389/fmars.2021.520713>
- Taylor, R. N., Murton, B. J., & Thirwall, M. F. (1995). Petrographic and geochemical variation along the Reykjanes Ridge, 57°N–59°N. *Journal of the Geological Society*, 152(6), 1031–1037. <https://doi.org/10.1144/gsl.jgs.1995.152.01.25>
- Vogt, P. R. (1971). Asthenosphere motion recorded by the ocean floor south of Iceland. *Earth and Planetary Science Letters*, 13(1), 153–160. [https://doi.org/10.1016/0012-821x\(71\)90118-x](https://doi.org/10.1016/0012-821x(71)90118-x)
- Waelbroeck, C., Labeyrie, L., Michel, E., Duplessy, J. C., McManus, J. F., Lambeck, K., et al. (2002). Sea-level and deep water temperature changes derived from benthic foraminifera isotopic records. *Quaternary Science Reviews*, 21(1–3), 295–305. [https://doi.org/10.1016/s0277-3791\(01\)00101-9](https://doi.org/10.1016/s0277-3791(01)00101-9)
- Weir, N. R. W., White, R. S., Brandsdóttir, B., Einarsson, P., Shimamura, H., & Shiobara, H. (2001). Crustal structure of the northern Reykjanes Ridge and Reykjanes Peninsula, southwest Iceland. *Journal of Geophysical Research*, 106(B4), 6347–6368. <https://doi.org/10.1029/2000jb900358>
- White, R. S., Bown, J. W., & Smallwood, J. R. (1995). The temperature of the Iceland plume and origin of outward-propagating V-shaped ridges. *Journal of the Geological Society*, 152(6), 1039–1045. <https://doi.org/10.1144/gsl.jgs.1995.152.01.26>
- Yeo, I. A., Devey, C. W., LeBas, T. P., Augustin, N., & Steinführer, A. (2016). Segment-scale volcanic episodicity: Evidence from the north Kolbeinsey Ridge, Atlantic. *Earth and Planetary Science Letters*, 439, 81–87. <https://doi.org/10.1016/j.epsl.2016.01.029>
- Yeo, I. A., & Searle, R. C. (2013). High-resolution remotely operated vehicle (ROV) mapping of a slow-spreading ridge: Mid-Atlantic Ridge 45°N. *Geochemistry, Geophysics, Geosystems*, 14(6), 1693–1702. <https://doi.org/10.1002/ggge.20082>

## References From the Supporting Information

- Bézos, A., & Humler, E. (2005). The Fe<sup>3+</sup>/ΣFe ratios of MORB glasses and their implications for mantle melting. *Geochimica et Cosmochimica Acta*, 69(3), 711–725. <https://doi.org/10.1016/j.gca.2004.07.026>
- Blichert-Toft, J., Agranier, A., Andres, M., Kingsley, R., Schilling, J., & Albarède, F. (2005). Geochemical segmentation of the Mid-Atlantic Ridge north of Iceland and ridge-hot spot interaction in the North Atlantic. *Geochemistry, Geophysics, Geosystems*, 6(1), Q01E19. <https://doi.org/10.1029/2004gc000788>
- Brooks, C. K., Jakobsson, S. P., & Campsie, J. (1974). Dredged basaltic rocks from the seaward extensions of the Reykjanes and Snaefellsnes volcanic zones, Iceland. *Earth and Planetary Science Letters*, 22(4), 320–327. [https://doi.org/10.1016/0012-821x\(74\)90141-1](https://doi.org/10.1016/0012-821x(74)90141-1)
- Campsie, J., Bailey, J. C., Rasmussen, M., & Dittmer, F. (1973). Geochemistry-Tholeiites from Reykjanes Ridge and Charlie (Gibbs) fracture zone. *Nature*, 244, 71.
- Christie, D. M., Carmichael, I. S. E., & Langmuir, C. H. (1986). Oxidation states of mid-ocean ridge basalt glasses. *Earth and Planetary Science Letters*, 79(3–4), 397–411. [https://doi.org/10.1016/0012-821x\(86\)90195-0](https://doi.org/10.1016/0012-821x(86)90195-0)
- Cohen, R. S., Evensen, N. M., Hamilton, P. J., & O'Nions, R. K. (1980). U–Pb, Sm–Nd and Rb–Sr systematics of mid-ocean ridge basalt glasses. *Nature*, 283(5743), 149–153. <https://doi.org/10.1038/283149a0>
- Gale, A., Dalton, C. A., Langmuir, C. H., Su, Y., & Schilling, J. (2013). The mean composition of ocean ridge basalts. *Geochemistry, Geophysics, Geosystems*, 14(3), 489–518. <https://doi.org/10.1029/2012GC004334>
- Hermes, O. D., & Schilling, J.-G. (1976). Olivine from Reykjanes ridge and Iceland tholeiites, and its significance to the two-mantle source model. *Earth and Planetary Science Letters*, 28(3), 345–355. [https://doi.org/10.1016/0012-821x\(76\)90196-5](https://doi.org/10.1016/0012-821x(76)90196-5)
- Hilton, D. R., Thirlwall, M. F., Taylor, R. N., Murton, B. J., & Nichols, A. (2000). Controls on magmatic degassing along the Reykjanes Ridge with implications for the helium paradox. *Earth and Planetary Science Letters*, 183(1–2), 43–50. [https://doi.org/10.1016/s0012-821x\(00\)00253-3](https://doi.org/10.1016/s0012-821x(00)00253-3)
- Jenner, F. E., & O'Neill, H. S. C. (2012). Analysis of 60 elements in 616 ocean floor basaltic glasses. *Geochemistry, Geophysics, Geosystems*, 13(2), Q02005. <https://doi.org/10.1029/2011gc004009>
- Johnson, G. L., & Jakobsson, S. P. (1985). Structure and petrology of the Reykjanes Ridge between 62°55'N and 63°48'N. *Journal of Geophysical Research*, 90(B12), 10073–10083. <https://doi.org/10.1029/jb090ib12p10073>

- Kelley, K. A., Kingsley, R., & Schilling, J. (2013). Composition of plume-influenced mid-ocean ridge lavas and glasses from the mid-Atlantic Ridge, East Pacific rise, Galápagos spreading Center, and Gulf of Aden. *Geochemistry, Geophysics, Geosystems*, 14(1), 223–242. <https://doi.org/10.1029/2012GC004415>
- Kempton, P. D., Fitton, J. G., Saunders, A. D., Nowell, G. M., Taylor, R. N., Hardarson, B. S., & Pearson, G. (2000). The Iceland plume in space and time: A Sr–Nd–Pb–Hf study of the north Atlantic rifted margin. *Earth and Planetary Science Letters*, 177(3–4), 255–271. [https://doi.org/10.1016/S0012-821X\(00\)00047-9](https://doi.org/10.1016/S0012-821X(00)00047-9)
- Kingsley, R. H., & Schilling, J.-G. (1995). Carbon in Mid-Atlantic Ridge basalt glasses from 28°N to 63°N: Evidence for a carbon-enriched Azores mantle plume. *Earth and Planetary Science Letters*, 129(1–4), 31–53. [https://doi.org/10.1016/0012-821X\(94\)00241-p](https://doi.org/10.1016/0012-821X(94)00241-p)
- Mattinson, J. M. (1978). 26. Lead isotope studies of basalts from IPOD Leg 49.
- Melson, W., & O'Hearn, T. (2003). Smithsonian volcanic glass file. Petrological Database of the Ocean Floor.
- Michael, P. J., & Schilling, J.-G. (1989). Chlorine in mid-ocean ridge magmas: Evidence for assimilation of seawater-influenced components. *Geochimica et Cosmochimica Acta*, 53(12), 3131–3143. [https://doi.org/10.1016/0016-7037\(89\)90094-x](https://doi.org/10.1016/0016-7037(89)90094-x)
- Moore, J. G., & Schilling, J.-G. (1973). Vesicles, water, and sulfur in Reykjanes Ridge basalts. *Contributions to Mineralogy and Petrology*, 41(2), 105–118. <https://doi.org/10.1007/bf00375036>
- Muehlenbachs, K., & Clayton, R. N. (1972). Oxygen isotope studies of fresh and weathered submarine basalts. *Canadian Journal of Earth Sciences*, 9(2), 172–184. <https://doi.org/10.1139/e72-014>
- O'Nions, R. K., & Pankhurst, R. J. (1974). Petrogenetic significance of isotope and trace element variations in volcanic rocks from the mid-Atlantic. *Journal of Petrology*, 15(3), 603–634. <https://doi.org/10.1093/petrology/15.3.603>
- Poreda, R., & Brozoldi, F. R. (1984). Neon isotope variations in Mid-Atlantic Ridge basalts. *Earth and Planetary Science Letters*, 69(2), 277–289. [https://doi.org/10.1016/0012-821X\(84\)90187-0](https://doi.org/10.1016/0012-821X(84)90187-0)
- Poreda, R., Schilling, J.-G., & Craig, H. (1986). Helium and hydrogen isotopes in ocean-ridge basalts north and south of Iceland. *Earth and Planetary Science Letters*, 78(1), 1–17. [https://doi.org/10.1016/0012-821X\(86\)90168-8](https://doi.org/10.1016/0012-821X(86)90168-8)
- Reekie, C. D. J., Jenner, F. E., Smythe, D. J., Hauri, E. H., Bullock, E. S., & Williams, H. M. (2019). Sulfide resorption during crustal ascent and degassing of oceanic plateau basalts. *Nature Communications*, 10(1), 82. <https://doi.org/10.1038/s41467-018-08001-3>
- Rowe, E. C., & Schilling, J.-G. (1979). Fluorine in Iceland and Reykjanes Ridge basalts. *Nature*, 279(5708), 33–37. <https://doi.org/10.1038/279033a0>
- Ryan, J. G., & Langmuir, C. H. (1987). The systematics of lithium abundances in young volcanic rocks. *Geochimica et Cosmochimica Acta*, 51(6), 1727–1741. [https://doi.org/10.1016/0016-7037\(87\)90351-6](https://doi.org/10.1016/0016-7037(87)90351-6)
- Schilling, J.-G. (1975). Rare-Earth variations across 'normal segments' of the Reykjanes Ridge, 60°–53°N, Mid-Atlantic Ridge, 29°S, and East Pacific Rise, 2°–19°S, and evidence on the composition of the underlying low-velocity layer. *Journal of Geophysical Research*, 80(11), 1459–1473. <https://doi.org/10.1029/jb080i011p01459>
- Shorttle, O., Moussallam, Y., Hartley, M. E., MacLennan, J., Edmonds, M., & Murton, B. J. (2015). Fe-XANES analyses of Reykjanes Ridge basalts: Implications for oceanic crust's role in the solid Earth oxygen cycle. *Earth and Planetary Science Letters*, 427, 272–285. <https://doi.org/10.1016/j.epsl.2015.07.017>
- Sigurdsson, H. (1981). First-order major element variation in basalt glasses from the mid-Atlantic Ridge: 29°N to 73°N. *Journal of Geophysical Research*, 86(B10), 9483–9502. <https://doi.org/10.1029/jb086ib10p09483>
- Tarney, J. (1979). Minor element geochemistry of basalts from Leg 49, north Atlantic Ocean. *Init. Rep. DSDP*, 49, 657–691.
- Unni, C. K. (1976). *Chlorine and bromine degassing during submarine and subaerial volcanism*. University of Rhode Island. Retrieved from <https://books.google.de/books?id=fNEywAACAAJ>
- Wood, D. A., Joron, J.-L., Treuil, M., Norrly, M., & Tarney, J. (1979a). Elemental and Sr isotope variations in basic lavas from Iceland and the surrounding ocean floor. *Contributions to Mineralogy and Petrology*, 70(3), 319–339. <https://doi.org/10.1007/bf00375360>
- Wood, D. A., Tarney, J., Varet, J., Saunders, A. D., Bougault, H., Joron, J. L., et al. (1979b). Geochemistry of basalts drilled in the north Atlantic by IPOD Leg 49: Implications for mantle heterogeneity. *Earth and Planetary Science Letters*, 42(1), 77–97. [https://doi.org/10.1016/0012-821X\(79\)90192-4](https://doi.org/10.1016/0012-821X(79)90192-4)
- Wood, D. A., Varet, J., Bougault, H., Corre, O., Joron, J. L., Treuil, M., et al. (1978). The petrology, geochemistry and mineralogy of north Atlantic basalts: A discussion based on IPOD leg 49. In *Initial report of deep sea drilling program* (Vol. 49, pp. 597–655). Retrieved from <https://cir.nii.ac.jp/crid/1570572700594475904>
- Zolotarev, B., Choporov, D. Y., & Voitov, G. (1979). Petrochemistry of basalts and distribution of organic gases: Holes 407, 408, 409, 410A, 411, 412, and 413, DSDP Leg 49. Luyendyk, BP, Cann, JR, et al., *Init. Repts. DSDP*, 49, 727–744.